

1 **Comparison of debris-flow observations, including fine sediment grain size and**
2 **composition, and runout model results at the Illgraben, Swiss Alps**

3
4
5 ^{1,2}Daniel Bolliger, ¹Fritz Schlunegger*, ³Brian W. McArdell

6
7 ¹Institute of Geological Sciences, University of Bern, Switzerland

8 ²Geotest AG, Zollikofen, Switzerland

9 ³Swiss Federal Institute WSL, Switzerland

10 *Corresponding author: fritz.schlunegger@unibe.ch

11
12
13 **Abstract**

14 Debris flows are important processes for the assessment of natural hazards due to their
15 damage potential. To assess the impact of a potential debris flow, parameters such as the
16 flow velocity, flow depth, maximum discharge and the volume are of great importance. This
17 study uses data from the Illgraben observation station, Central Alps of Switzerland, to explore
18 the relationships between these flow parameters and the debris flow dynamics. To this end,
19 we simulated previous debris flow events with the RAMMS debris flow runout model, which is
20 based on a numerical solution of the shallow water equations for granular flows using the
21 Voellmy friction relation. Here, the events were modeled in an effort to explore possible
22 controls on the friction parameters μ and ξ , which describe the Coulomb friction and the
23 turbulent friction, respectively, in the model. Additionally, sediment samples from levee
24 deposits were analyzed for their grain size distributions (14 events) and their mineralogical
25 properties (four events) to explore if the properties of the fine-grained matrix have an influence
26 on the debris flow dynamics. Finally, field data from various debris flows such as the flow
27 velocities and depths were statistically compared with the grain size distributions, the
28 mineralogical properties, and the simulation results to identify the key variables controlling the
29 kinematics of these flows. The simulation results point to several ideal solutions, which depend
30 on the Coulomb and turbulent friction parameters (μ and ξ , respectively). In addition, the
31 modelling results show that the Coulomb and turbulent frictions of a flow are related to the
32 Froude number if the flow velocity is $< 6-7$ m/s. It is also shown that the fine-sediment grain
33 size or clay-particle mineralogy of a flow neither correlates with the flow's velocity and depth,
34 nor can it be used to quantify the friction in the Voellmy friction relation. This suggests that the
35 frictional behavior of a flow may be controlled by other properties such as the friction generated
36 by the partially fluidized coarse granular sediment. Yet, the flow properties are well-correlated

37 with the flow volume, from which most other parameters can be derived, consistent with
38 common engineering practice.

39 **1 Introduction**

40 *1.1 Debris flows, and parameters controlling their velocity and runout*

41 Debris flows are rapid mass movements consisting of water-saturated and poorly sorted
42 debris with a large range of grain sizes. Debris flows tend to develop one single or a suite of
43 multiple surges with steep coarse-grained fronts. Their motion is driven by gravity and resisted
44 by friction within the flow and at the boundary with the channel bed (Iverson, 1997). The
45 boulder-rich front is then followed by a tapering body where the pore fluid pressures are large,
46 often exceeding the hydrostatic pressure (Iverson, 1997, McArdell et al., 2007). In the frontal
47 part, larger particles tend to ascend in the debris flow body due to particle collisional stresses
48 thereby building a coarse-grained top layer (Johnson et al., 2012), which travels somewhat
49 faster than the flow front itself, delivering coarse sediment to the front. Accordingly, the
50 coarser-grained particles along with some of the fine sediment present at the surface of the
51 flow tend to accumulate in the surge head and are deposited laterally in levees just a few
52 meters behind the front (Johnson et al., 2012).

53 In the past years, de Haas et al. (2015) conducted experiments to investigate how the grain
54 size distribution and water content influences the velocity of a debris flow. They found that a
55 higher clay content tends to result in an increase of both the velocity and the runout distance
56 of such flows. However, if the clay content becomes too large, then the velocity decreases
57 due to a higher viscosity of the fluid. This relationship should also be applicable to the silt
58 fraction because clay and silt particles are a part of the fluid while grains larger than silt
59 contribute to the solids of a debris flow (Iverson, 1997). The experiments of de Haas et al.
60 (2015) also showed that a large gravel content in the flow front leads to a strong frictional
61 resistance, which in turn reduces the flow velocity. In addition, a large gravel content results
62 in a larger pore water diffusivity, which reduces the pore pressure in the flow and contributes
63 to a further reduction of the flow velocity. On the other hand, a low gravel content leads to
64 lower collisional forces, which might also lead to a relatively low flow velocity. Furthermore,
65 also according to the experiments by de Haas et al. (2015), the water content, the velocity,
66 the volume, and the runout distance of a debris flow are positively correlated to each other.
67 Based on a combination of experimental and field data, Hürlimann et al. (2015) came to the
68 same conclusions, and they additionally found that an increase in the clay content generally
69 leads to a reduction in the runout distance. Indeed, the absorption of water in swelling clay
70 minerals has the potential to result in an increase of the cohesion of a flow, which in turn could
71 cause a reduction of the flow velocity and the runout distance. Finally, using laboratory
72 experiments, Kaitna et al. (2016) documented that a relatively high fraction of fine-grained
73 material tends to occur in flows with excess pore fluid pressures. In addition, these authors
74 mentioned that such flows were characterized by low fluctuations of normalized fluid pressures
75 and normal stresses, and the experiments showed that the shear stresses were concentrated

76 at the base of the flow. Based on the conclusions of the aforementioned authors, we expect
77 to see a dependency of the flow properties in the Illgraben and the granulometric composition
78 of these flows (Uchida et al., 2012), and we anticipate that the flow velocity is negatively
79 correlated with the relative abundance of the finest-grained particles.

80 The mineralogical composition of a flow is a further parameter, which has the potential to
81 impact the rheology and thus the flow velocity and runout distance of debris flows, yet these
82 relationships have largely been overlooked in the literature. In particular, because clay
83 minerals are important constituents of the fine-grained fraction of these flows, they have the
84 potential to regulate the pore fluid pressure and the stress state through their ability to absorb
85 water in their crystal structure (Di Maio et al., 2004). This is mainly the case for swelling clay
86 minerals (see also section above) such as those of the smectite group (Di Maio et al., 2004),
87 where the pore fluid composition has a large influence on the volume and the shear strength
88 of these minerals (Chatterji and Morgestern, 1990; Di Maio, 1996). Because shear stresses
89 within a flow are a direct consequence of the friction between the particles and the fluid phase
90 and since the friction properties directly influence the propagation of a debris flow (see section
91 1.2), we anticipate the occurrence of a direct relationship between the velocity and runout
92 distance of debris flows, and the mineralogical composition of the fine-grained matrix.

93

94 *1.2 Physically-based models describing debris flow processes, and goal of paper*

95 There are several rheological models or flow resistance relationships describing the behavior
96 of debris flows such as the flows' velocities, runout distances and frictional properties (e.g.,
97 Allen, 1997; Rickenmann, 1999; Naef et al., 2006). One commonly used approach is the
98 Voellmy friction relation (Voellmy, 1955; Salm, 1990; 1993; Christen et al., 2012), which is
99 also implemented in the software RAMMS, a software package to simulate debris flow runout
100 (see section 3.1). In the Voellmy friction equation, the frictional resistance of a flow S [Pa] is
101 composed of the sum of two friction terms: (i) A dry Coulomb-type friction term, referred to as
102 Coulomb friction, describes the frictional resistance between the debris flow and the channel
103 bed and mainly depends on the flow depth; and (ii) a drag or viscous-turbulent friction term
104 describes the turbulent frictional resistance, which mainly depends on the dynamic pressure
105 and thus on the velocity of the flow. Both components are characterized by the coefficients μ
106 and ξ , which control the values of the Coulomb and the turbulent frictions, respectively
107 (Christen et al., 2012). Optionally, cohesion stresses can be included in an extended Voellmy
108 friction equation (Bartelt et al., 2015; Berger et al., 2016). Because this additional cohesion
109 term has rarely been used in engineering practice and is apparently relatively small (Berger
110 et al., 2016), it was neglected herein, and the friction equation takes the following form:

$$111 \quad S = \mu N + \frac{\rho g v^2}{\xi}, N = \rho g h \cdot \cos(\varphi) \quad (1),$$

112 where S is the frictional resistance [Pa], ρ the density of the debris flow, h the flow height (or
113 flow depth), g the gravitational acceleration, φ the slope angle of the channel bed, and v the
114 velocity of the flow.

115 A simplified approach to characterize a debris flow is the Froude number, which describes the
116 ratio between the inertial and the gravitational forces:

$$117 \quad Fr = \frac{v}{\sqrt{gh}} \quad (2),$$

118 where Fr is the Froude number, v the velocity of the flow, g the gravitational acceleration and
119 h the flow height (Hübl et al., 2009; Choi et al., 2015).

120 As mentioned above, the velocity and runout distance of debris flows are likely to depend on
121 the frictional resistance in such mass movements. This friction, in turn, can be characterized
122 by two coefficients μ and ξ in the Voellmy friction relation (1). Because we anticipate that the
123 mineralogical and granulometric composition of the fine-grained matrix has an influence on
124 the properties of such flows (see section 1.1), we expect to identify a relationship between the
125 frictional properties of a flow, its velocity, and its grain size and mineralogical composition.
126 Here, we test and explore these hypotheses using in-situ data collected at the Illgraben debris
127 flow monitoring station situated in the Central European Alps (Figure 1), and we evaluate the
128 data with the results of a numerical runout model referred to as RAMMS. Upon combining field
129 data with modelling results, we aim at identifying those parameters that have the largest
130 control on the dynamic properties of the debris flows at the Illgraben.

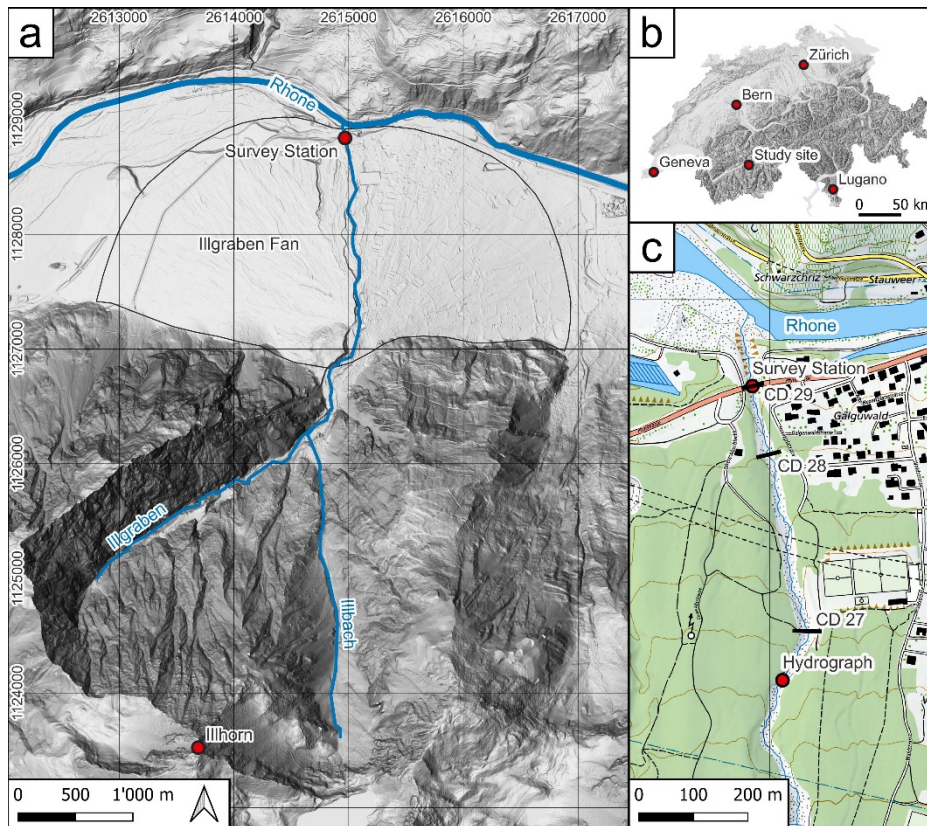
131

132 **2 Study site and setting**

133 The Illgraben catchment is located in the Valais region in western Switzerland (Figure 1). It
134 extends from the summit of the Illhorn (2716 m asl) to the outlet of the Illgraben into the Rhone
135 River (610 m asl). The total area of about 9.5 km² consists of the Illgraben basin, which has a
136 spatial extent of 4.6 km², and the Illbach tributary catchment covering 4.9 km² (Figure 1a). The
137 Illgraben basin has been very active and has generated several debris flows each year
138 (Schlunegger et al., 2009; McArdell and Satori, 2022). The rates of sediment discharge in the
139 Illgraben have been exceptionally high for Alpine standards (Berger et al., 2011a). Several
140 studies showed that the erosion rates and the numbers and extents of debris flows strongly
141 depend on the hydro-climatic parameters such as the average annual temperature and the
142 precipitation rates (Bennett et al., 2013; Hirschberg et al., 2019; 2021a, b). The highly fractured
143 bedrock (Bumann, 2022), belonging to the Penninic nappe stack (Gabus et al., 2008), consists
144 of massive-bedded limestones, quartzites and Triassic schists with dolobreccia interbeds.
145 Schlunegger et al. (2009) considered these lithologies to be the main source of the silt and
146 clay fraction that constitute the matrix of the debris flow deposits. Based on a petrographic
147 analysis of the debris flow deposits, these authors also identified two distinct sediment sources

148 in the Illgraben where bedrock lithologies with different petrological properties are exposed.
149 These are (i) a heavily fractured and foliated suite of gneisses and schists, which are exposed
150 on the southern flank of the Illgraben, and (ii) a vertically plunging succession of limestones,
151 dolomites and cellular dolomites, which make up the northwestern flank of the Illgraben
152 (Figure 1). The material from these two sources is very well mixed in response to repeated
153 deposition and remobilization of sediment within the catchment (Schlunegger et al., 2009).
154 The sediment cascade has been subject to seasonal variations, where smaller debris flows
155 events are associated with net sediment accumulation in the channel, while large flows can
156 entrain sediment up to several times their initial mass along their flow paths (Berger et al.,
157 2010; Berger et al., 2011a, b; Schürch et al., 2011).

158 Grain size analyses conducted on samples from the channel bed and debris flow deposits
159 indicated sand contents of 35-40% and clay contents of < 5% (Hürlimann et al., 2003;
160 Schlunegger et al., 2009; Uchida et al., 2021). In the Rhone valley, an alluvial fan has formed
161 covering an area of 6.6 km² (Schürch et al., 2016). The channel on the fan has a U-shaped
162 cross-sectional geometry with a base that is about 5–10 m wide. For the lowermost 2 km, the
163 gradient of the Illgraben channel ranges from about 7% to 18% (measured over a length of 50
164 m) with a mean of about 8% (Schlunegger et al., 2009). Thirty-one check dams with vertical
165 drops of up to several meters were constructed along the lowermost 4.8 km of the channel to
166 prevent the flows to further incise into the substratum (McArdell et al., 2007; Badoux et al.,
167 2009). A debris flow monitoring station, situated on the lower fan c. 200 m upstream of the
168 confluence with the Rhone River, was installed in 2000 and has been operated by the WSL
169 since then (Hürlimann et al., 2003; Badoux et al., 2009). At the survey site (Figure 1c), the
170 measured parameters include frontal velocity, flow depth, bulk density, maximum discharge
171 rate, volumes, and normal and shear force (McArdell et al., 2007; McArdell 2016). The related
172 values are presented in the openly accessible database of the WSL (McArdell et al., 2023),
173 and the data was collected using the methods presented in section 3.1. On average 3 to 5
174 debris flows have been registered by the measuring station every year. They have generally
175 occurred during intense rainstorms between May and October (e.g., McArdell et al., 2007).
176



177

178

179

180

181

182

183

184

Figure 1: (a) Overview of the topographic situation around the Illgraben showing the Illgraben system with its river network consisting of the Illgraben, Illbach and the Rhone River. (b) Overview map of Switzerland with location of the study site. (c) Detailed topographic map of the Illgraben reach along which the RAMMS simulations have been conducted. It shows the location of the input hydrograph which was used as starting position for the modelling. The three check dams (CD) and the location of the survey station below the Pfyenstrasse are displayed on this figure. The background is provided by the swissALTI3D and the Swiss Map Raster 10 (Swisstopo, 2022).

185 3 Methods

186

187

188

189

190

191

192

193

194

195

196

197

198

199

200

Using data collected in the field (section 3.1), we explored how the frictional properties of a debris flow influences the behavior (flow depth and velocity) of such a flow through modelling with RAMMS (section 3.2). We then tested whether the grain size distribution (section 3.3) and the mineralogical composition of the debris flow material (section 3.4) have an influence on the flow velocity.

3.1 Surveys of debris flows

Many of the in-situ measurements of the debris flow properties at the Illgraben have been accomplished with a force plate that is installed in the channel beneath a bridge c. 200 m upstream of the confluence with the Rhone River (survey station, see Figure 1c). At that survey site, information on (i) the velocity, (ii) the flow depth, (ii) the mean bulk density, (iii) the duration of individual debris flows, and (iv) the volumes of each flow have been determined in the past years by the WSL (e.g., McArdell and Sartori, 2021; de Haas et al., 2022, Belli et al., 2022; McArdell et al., 2023). As outlined in McArdell et al. (2007) and Schlunegger et al. (2009), the force plate is a horizontal 8 m² steel structure, which is installed flush with the river

201 bed just on the top of the concrete check dam. The plate is equipped with normal and shear
202 force transducers. The flow depth is estimated using either a laser or radar unit. Because the
203 radar data is biased by an unpredictable smoothing of the flow surface, we preferentially used
204 the laser data for further calculations. Based on information about the flow depth and the
205 normal force, it was possible to determine the bulk density of a flow as it moves on the plate
206 itself. The volume of each flow was then calculated as the product between the velocity and
207 the cross-sectional area, and this product was integrated over the flow's duration (McArdell et
208 al., 2023). The frontal velocity is determined using the travel time of the flow front over the
209 reach upstream of the force plate (between check dams 27 or 28 and 29; Figure 1c and
210 Hürlimann et al., 2003). Appendix A presents a list of parameters, which been measured at
211 the Illgraben monitoring site, and Appendix B for screenshots from video recordings of
212 selected debris flows.

213

214 3.2 Numerical modelling with RAMMS

215 We explored, through modelling with RAMMS, how the frictional properties of a debris flow
216 influence its behavior such as flow depth and velocity. The RAMMS model was developed by
217 the Swiss Federal Institute for Forest, Snow and Landscape Research, WSL (WSL, 2022). It
218 is based on the two-parameter Voellmy-fluid model (Christen et al., 2012; Bartelt et al. 2015),
219 which describes the friction in the 2D depth-averaged equations of motion, which were
220 deviated for granular flows. We justify the selection of such an approach because in an
221 independent modelling study (FLATModel) calibrated with field data (Medina et al., 2007), the
222 Voellmy-fluid formula (eq. 1) has been proven to reproduce the dynamics of debris flows (flow
223 velocity, erosion pattern in the channel, and aerial extension of the flow in the accumulation
224 zone) reasonably well. A major challenge for modelling is the choice of the input friction
225 coefficients. In particular, if the simulation cannot be calibrated with data that were collected
226 from a previous well-documented event (Christen et al., 2012; Deubelbeiss & Graf, 2011), the
227 input parameters have to be estimated. Because the model results such as the velocity, the
228 runout distance, and the flow depth are sensitive to the friction parameters μ and ξ (Bartelt et
229 al., 2015; Christen et al., 2012), we iteratively changed the values of these coefficients until
230 we found, for each event, a best fit between the simulation results and the observations
231 (Appendix C).

232 The Coulomb friction coefficient μ is sometimes expressed as the tangent of the internal shear
233 angle (WSL, 2022). According to Salm (1993) an internal movement parallel to the slope is
234 only possible if the internal shear angle is smaller than the slope angle. Consequently, the
235 value of μ should be smaller than the tangent of the channel slope angle. For a minimum slope
236 angle of 7% (4°), μ should thus be smaller than 0.07. Therefore, for every debris flow event,
237 we conducted several simulations (between 12 and 43, Appendix C) with μ varying from 0.01

238 to 0.06, and we modified the ξ parameter to minimize the z-value, which is explained with eq.
239 (3) below. This resulted in μ - ξ pairs with lowest z-values and thus best fits between the model
240 results and observations (such as the flow velocity v and the flow depth h). Please see
241 Appendix C for information about the number of modelling runs, the intervals between the μ -
242 and ξ -values, and other input parameters that we used upon modelling.

243 We employed the 'hydrograph' input option of RAMMS to characterize the debris flows in the
244 model. Upon modelling, the hydrograph input was placed c. 500 m upstream of the survey site
245 (check dam 27, Figure 1c). Erosion was allowed to occur along the entire channel (Frank et
246 al., 2015; 2017) except at the check dams. Similar to the surveys in the field (section 3.1), the
247 model velocity was calculated using the travel time between check dams 28 and 29 (Figure
248 1c). The modelled flow depth values used herein were obtained as the average of the
249 measurements that were conducted at four points along a cross section at check dam 29.

250 The use of RAMMS requires a digital elevation model (DEM), event volume, and peak
251 discharge. The drone-based DEM, which is based on a survey conducted on the 10th of August
252 2021 (de Haas et al., 2022), was used for all simulations. However, this high-resolution DEM
253 did not cover the section of the channel between the Survey Station and the Rhone River
254 (Figure 1c). Therefore, in order to extend the area towards the confluence with the Rhone
255 River, the photogrammetry DEM, which has resolution of 0.1 m, was combined with an existing
256 0.5 m-lidar DEM (Swisstopo, 2022) using the software QGIS. Here, we resampled the drone-
257 based DEM to achieve the same resolution as the lidar DEM of Swisstopo (i.e., 0.5 m) so that
258 both datasets could be combined. The DEM of the short, concrete channel section beneath
259 the road bridge had to be reconstructed manually because it was not possible to image the
260 topography below the bridge. In addition, a filter (Serval-Raster editing tools, version 3.10.2)
261 was applied to the channel bed to smoothen the bed surface. This was done because a large
262 local change in the topography (such as a boulder) can induce strong vertical accelerations in
263 RAMMS (and other models that are based on the depth-averaged equations of motion), which
264 can lead to unrealistically large (or small) local flow depths.

265 Finally, we introduced a dimensionless z-value to describe the deviation of the simulated
266 velocity v and flow depth h from the measurements in the field:

$$267 \quad z = \sqrt{\left(\frac{v_{simulation} - v_{measured}}{v_{measured}}\right)^2 + \left(\frac{h_{simulation} - h_{measured}}{h_{measured}}\right)^2} \quad (3).$$

268 We thus explored how the model input parameters (μ - and ξ -values) affect the modelled
269 velocity and depth values of a flow. We then compared the model results with the surveyed
270 velocities and depths of each flow using eq. (3), which we implemented in the software Matlab
271 (R2021b).

272

273 3.3 *Grain size distribution*

274 For most of the debris flows that occurred in the years 2019, 2021 and 2022, at least one
275 sediment sample of 1.5 to 3 kg was taken from the levee deposits at the same site labelled as
276 'Survey Station' in Figure 1c (Swiss coordinates: 2'614'973, 1'128'842; Figure 1c). We
277 collected the material from underneath the bridge to prevent effects related to grain-size-
278 dependent erosion by rainfall. We selected the levee deposits for three reasons. First,
279 according to our experience, the levee deposits can better be attributed to a specific event
280 than other sediments of a debris flow. Second, the levee deposits are those sediments of a
281 debris flow that most clearly record the granulometric composition of the surge head, as our
282 observations on video recordings have shown. Third, it is the surge head, which exerts the
283 greatest control on the dynamics of a debris flow (McArdell et al., 2007; Johnson et al., 2012).
284 Accordingly, upon collecting material from levee deposits, we are likely to analyze sediments
285 with the highest potential to provide information that allows us to understand the dynamics
286 (e.g., flow depth and velocity) of past debris flows. Yet we acknowledge that this material is
287 more likely coarser grained than the sediments in the tail of such a flow (McArdell et al., 2007).
288 In the laboratory, all of the collected material was processed following the state-of-the-art
289 protocol (SN670 004–2b–NA norm), which was established at the Bern University of Applied
290 Sciences (Burgdorf). Following this protocol, the material was first dried and then sieved to a
291 minimum particle size of 0.5 mm using a set of 7 sieves, each of which has a defined mesh
292 size: 31.5 mm, 16 mm, 8 mm, 4 mm, 2 mm, 1 mm, and 0.5 mm. Subsequently, a slurry analysis
293 was carried out on the material < 0.5 mm using a hydrometer. The goal of this task was to
294 determine the particle size distribution between 0.1 and 0.001 mm. Finally, the grain size
295 distribution of the remaining material between 0.5 and 0.063 mm was determined by wet
296 sieving. During this task, we used three sieves where the mesh size was 0.25 mm, 0.125 mm
297 and 0.063 mm. The grain size distribution was truncated at 16 mm so that the entire sample
298 is at least 100 times the mass of the largest particle (e.g., Church et al., 1987). We note,
299 however, that particles larger than 16 mm do occur on the levee deposits and we did sample
300 such material in the field. However, we were not able to consider this fraction due to technical
301 limitations in our laboratory and practical limitations on the mass of the sample necessary for
302 analysis.

303

304 3.4 *Powder XRD*

305 We hypothesize that clay minerals influence the pore pressure of a flow (Barshad, 1952),
306 which in turn could influence its mobility (McArdell et al., 2007). We expect such a control
307 because swelling clays tend to absorb water in their crystal structure. The result is an increase
308 in the viscosity of the flow, thereby reducing the dissipation of the fluid pore pressure. To test
309 this hypothesis, the mineralogical properties of some debris flow samples were measured

310 through standard powder XRD at the Institute of Geological Sciences of the University of Bern.
 311 For this purpose, four samples were chosen from fast and slow velocity flows as well as from
 312 deposits where either the coarse-grained or the fine-grained fractions dominate in the
 313 analyzed grain size spectrum. To this end, the grain size fraction < 0.063 mm, which was
 314 already extracted during the steps outlined above, was analyzed for powder XRD. Subsequent
 315 milling with a vibrating-disc mill (Retsch RS 200) and a McCrone XRD-mill reduced the particle
 316 sizes to the sub-micrometer scale. Corundum powder was added as standard to the samples,
 317 and the samples were measured with the x-ray diffractometer X'Pert Pro MPD with Cu
 318 radiation. Because this step did not include a determination of the mineralogic composition of
 319 the clay minerals, a slightly different approach had to be employed. Here, we used the same
 320 initial material, but it was only milled with the vibrating disc mill. The powder was then mixed
 321 with a dispersant (0.1 molar NH_3) to achieve a homogeneous suspension. The clay particles
 322 were separated in an Atterberg cylinder. The particles still in suspension after 15 hours were
 323 extracted using a centrifuge. The extracted clay particles were then cleaned with HCl, CaCl_2
 324 and deionized water. To distinguish between the different clay minerals, three sample holders
 325 were either air dried, treated with ethylene glycol or heated to 400°C and 550°C before
 326 measuring with the X'Pert Pro MPD with Cu radiation. The final processing of the data was
 327 carried out with the software TOPAS (Coelho, 2018), which uses a Rietveld structure
 328 refinement technique (Rietveld, 1969).

329

330 4 Results

331 4.1 Survey results

332 A total of 13 events from 2019, 2021, and 2022 were analyzed (Appendix A, Table 1). The
 333 measured flow velocities varied by one order of magnitude from 0.89 m/s to 8.69 m/s. The
 334 maximum flow depths ranged from 1.13 m to 3.13 m, and the Froude numbers spanned the
 335 interval between 0.27 to 2.35, pointing towards considerable differences in the dynamics of
 336 these flows. The total volumes reached a maximum of c. $176,000 \text{ m}^3$ and the maximum
 337 discharge rate was c. $190 \text{ m}^3/\text{s}$. The measured density ranged from 1189 kg/m^3 to 2323 kg/m^3 ,
 338 and the corresponding volumetric water contents were between c. 20% and 90%.

339

340 Table 1: Measured and analyzed debris flow events from 2019, 2021, and 2022. Velocity, flow depth, volume,
 341 maximum discharge (Q_{max}) and density are the results of direct measurements at the monitoring station in the
 342 Illgraben (Figure 1c). The Froude number was derived from these. The last two columns show, for which events
 343 XRD analyses and RAMMS simulations were performed. The event of the 26th of July 2019 could not be simulated
 344 due to the high Froude number.

Event date	Velocity [m/s]	Flow depth [m]	Froude number []	Volume [m^3]	Q_{max} [m^3/s]	Density [kg/m^3]	XRD analysis	RAMMS simulation
21.06.2019	6.62	3.13	1.19	97394	147.61	1870		✓
02.07.2019	3.86	1.75	0.93	73188	65.58	1971	✓	✓
26.07.2019	8.69	1.39	2.35	113310	93.26	2223	✓	

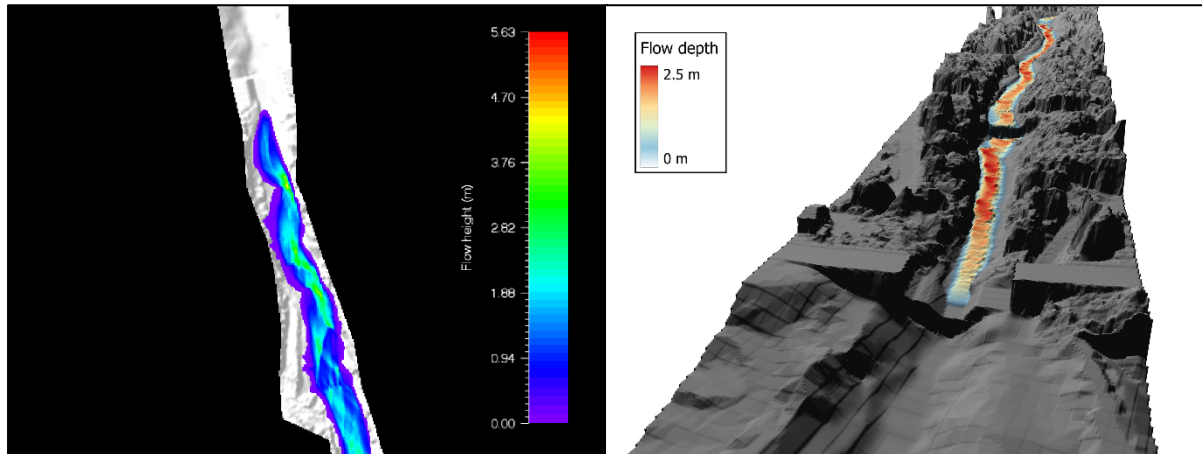
11.08.2019	6.95	1.81	1.65	88064	95.63	2323		✓
20.08.2019	0.89	1.13	0.27	6137	8.06	2031	✓	✓
24.06.2021	8.18	2.40	1.69	105032	162.20	1750		✓
06.07.2021	8.69	2.50	1.75	76906	186.61	1605		✓
16.07.2021	2.78	2.38	0.58	80879	60.70	1916	✓	✓
07.08.2021	2.32	2.49	0.47	38737	41.19	1884		✓
19.09.2021	1.25	1.13	0.38	8538	10.67	1697		✓
05.06.2022	3.39	2.08	0.75	39498	55.42	1690		✓
04.07.2022	8.18	2.49	1.66	175929	169.14	1189		✓
08.09.2022	1.91	1.93	0.44	9283	20.94	1592		✓

345

346 4.2 Numerical modelling with RAMMS

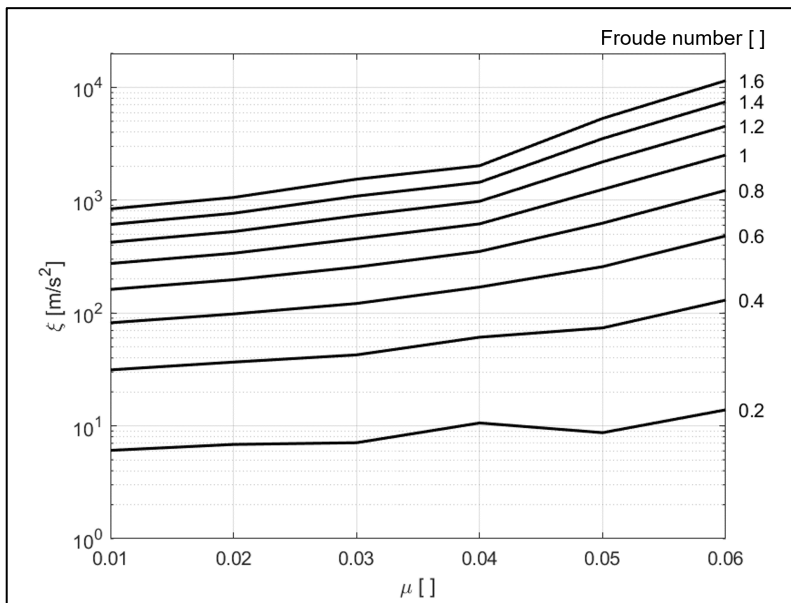
347 As mentioned above, we iteratively changed the μ - and ξ -friction values upon modelling until
348 we found a best-fit between the modelled and observed flow velocity and flow depth of each
349 flow (Appendix C and D). Because the latter properties of a debris flow (velocity and depth)
350 can be characterized by the Froude number (defined by eq. (2)), we first describe the
351 dependency of the modelled flow pattern on the Froude number, which itself is calculated
352 using the flow depth and velocity data of the field survey (Table 1). Please note that in this
353 context, eq. (2) predicts that changes in the flow velocity have a larger impact on the Froude
354 number than variations in flow depth. The simulations showed that RAMMS produces
355 reasonable results (e.g., Figure 2) for Froude numbers up to about 1.75 (Table 1). For larger
356 values (e.g., flows with large flow velocities), the simulations predict the occurrence of
357 standing waves at the debris flow front, which, however, have not been observed at the
358 Illgraben. Therefore, no simulations were possible for the event on the 26th of July 2019,
359 because this flow was characterized by a Froude number of 2.35. We acknowledge that roll-
360 waves, which could correspond to the standing waves simulated by RAMMS, do occur in a
361 debris flow, but such waves are mainly observed in the debris flow body and not at the
362 bouldery front.

363



364
365
366
367
368

Figure 2: Example of simulated flow depths. The image on the left shows flow depths in a 2D view provided by the RAMMS software. The image on the right shows a 3D view of the debris flow projected on a hillshade model using the QGIS software.

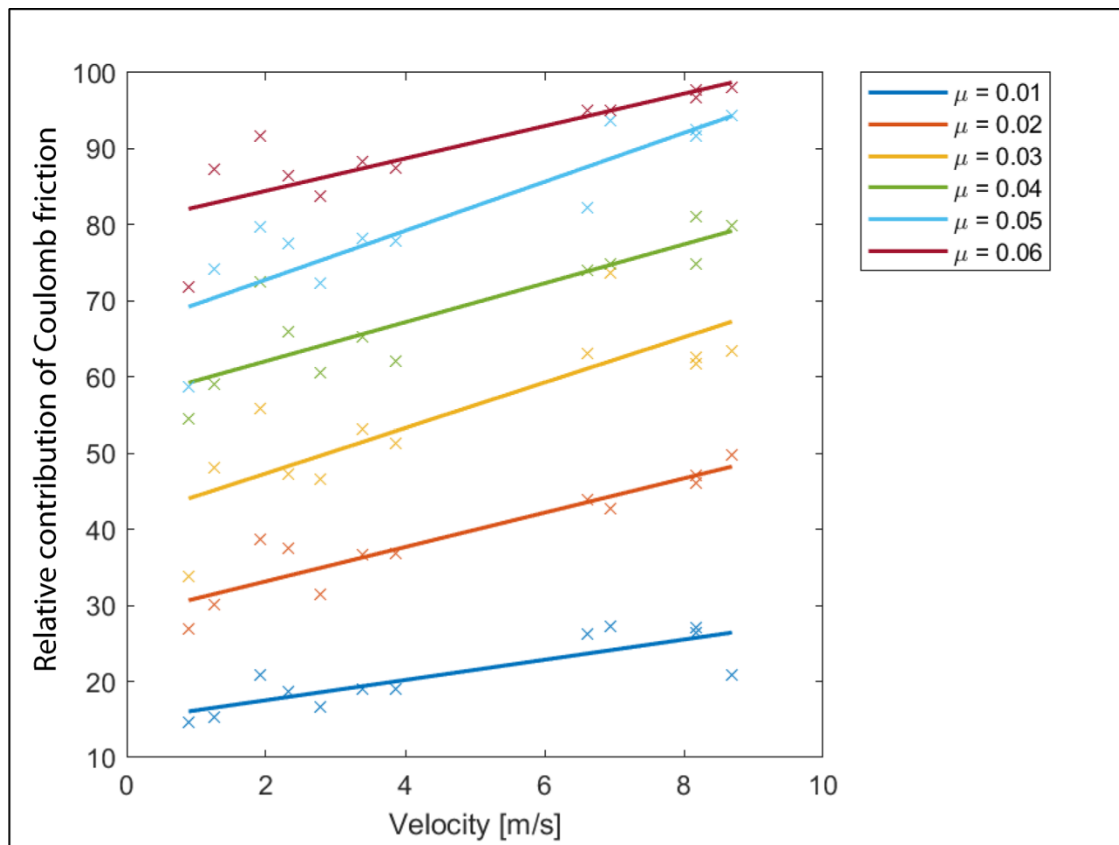


369
370
371
372
373

Figure 3: Modelled μ - ξ pairs, which result in a best fit between the observed and the modelled debris flow parameters. These latter values, in turn, appear to depend on the Froude numbers (based on measurements in the field, see Table 1) of the corresponding debris flow events.

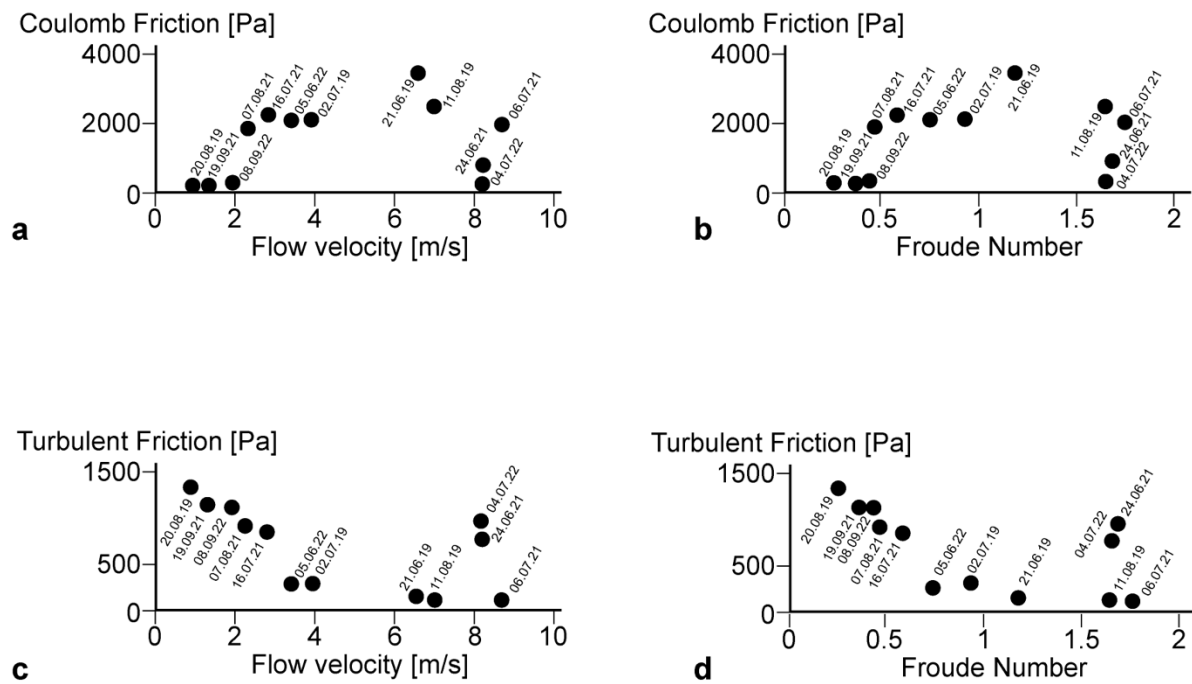
374 The model results show that more than one best-fit μ - ξ pair is possible for successfully
375 reproducing the observed velocity and depth of a flow (Appendix E). Yet, on average, the
376 lowest z-value is calculated for the μ - ξ pair with $\mu = 0.01$, followed by the pairs with $\mu = 0.02$
377 and $\mu = 0.05$. These values and patterns are consistent with the results of other debris flows
378 analyses conducted with RAMMS and applied to observations in e.g., the Alps (see Mikoš and
379 Bezak, 2021, for an overview of related papers), the Himalayas near Luzhuang in China
380 (Jianjun and Zhang; μ - and ξ -values of 0.07 and 1500 m/s²), and the coastal region in the
381 vicinity of Western Ghats in India (Abraham et al., 2021; μ - and ξ -values of 0.01 and 100
382 m/s², respectively). In addition, Simoni et al. (2012) found that RAMMS successfully
383 reproduced the maximum observed runout distances of debris flows in the Italian Alps for μ -

384 values close to the energy gradient of the debris flow channel (which is the tangent of the
 385 surface slope). Our modelling results support these inferences and additionally show that the
 386 modelled μ - and ξ -relationships show a strong dependency on the corresponding Froude
 387 numbers calculated from the field data (Figure 3, and Appendix E, F). Besides, for a given μ -
 388 value, the RAMMS models predict that the ξ -values increase with the Froude number. Such
 389 an increase is more obvious for large than for small μ -values (Figure 3, see also Appendix F).
 390



391
 392 Figure 4: Correlations between the relative contribution of the Coulomb friction to the total friction in
 393 percent (y-axis) and the velocity of a debris flow (x-axis) for different μ -values. The data points refer to
 394 best-fit simulations only. The lines are first order polynomial least square fitted trendlines.

395 Figure 4 illustrates that upon modelling, the relative contribution of the Coulomb friction to the
 396 total friction increases with the flow velocity, and it shows that this contribution is greater for
 397 large μ -values than for small ones. In particular, while the percentages of the Coulomb friction
 398 are in the range of c. 20% for a μ -value of 0.01 and a flow velocity of < 1 m/s, they increase to
 399 > 90% for a larger μ -value of 0.06 and a flow velocity of > 8 m/s.



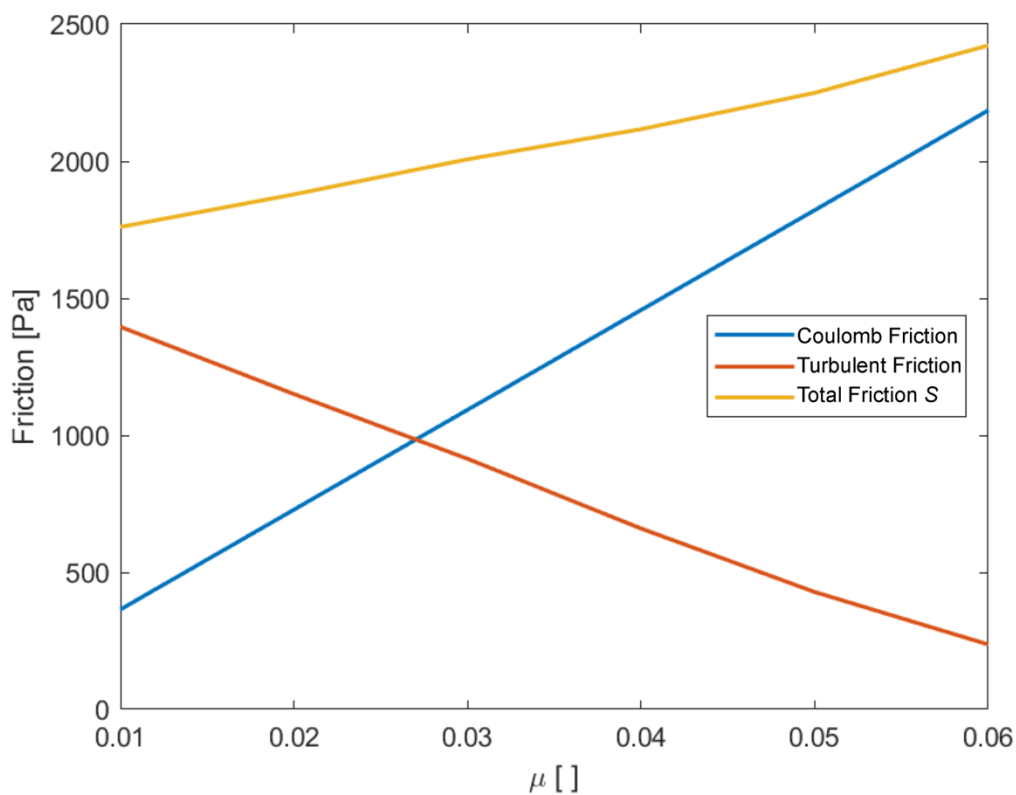
400

401 Figure 5: Relationships between a) flow velocity and Coulomb friction, b) Froude number and
 402 Coulomb friction, c) flow velocity and turbulent friction, and d) Froude number and turbulent friction.
 403 The plots show the results of the best-fit simulations for each flow.

404 The relationships elaborated above are further detailed in Figure 5, which documents the
 405 dependency of the friction property (Coulomb and turbulent friction) of a flow on its velocity
 406 and the corresponding Froude number. Note that for this analysis, we only considered the
 407 results of the best-fit simulations of each flow. Accordingly, rapid debris flows with high Froude
 408 numbers tend to be characterized by a large Coulomb friction, while slower debris flows are
 409 simulated more reliably with a rather low Coulomb friction (Figures 5a, 5b). Conversely, flows
 410 with a slow velocity tend to have a larger turbulent friction and are characterized by a low
 411 Froude number, whereas the turbulent friction tends to be low for flows with a high velocity
 412 and a high Froude number (Figures 5c, 5d). However, we note that the aforementioned
 413 relationships between flow velocity, Froude number, turbulent and Coulomb friction break
 414 down for flows that are more rapid than c. 6-7 m/s (Figure 5). Similar to the event on 26th of
 415 July 2019, these flows are characterized by Froude numbers that are much larger than 1
 416 (Table 1). These flows appear to be in a condition in which the relationships between friction
 417 and flow properties are apparently non-linear and more complex than in flows, which can be
 418 characterized by low Froude numbers. A further elaboration of this topic is, however, beyond
 419 the scope of this paper.

420 Figure 6 summarizes the consequences of the aforementioned relationships. In particular,
 421 small values of the Coulomb friction coefficient ($\mu \sim 0.01$), when the flow is moving on the
 422 order of a few meters per second, indicate that the contribution of the Coulomb term to the
 423 total friction is small, and that the total friction is therefore dominated by the turbulent friction

424 term (Figure 6). In the extreme case when $\mu = 0$, the turbulent friction term (eq. 1) closely
 425 resembles a Chezy friction from open-channel hydraulics (e.g. Henderson, 1966). Large
 426 values of the Coulomb friction coefficient (here $\mu \sim 0.05$) suggest that the Coulomb friction
 427 term is important, and that the contribution of the turbulent friction is correspondingly less
 428 significant (Figure 6). Because we found ideal μ - ξ pairs with $\mu = 0.01$ – 0.02 and $\mu = 0.05$ for
 429 most debris flows, we considered these flows to be dominated either by (i) the turbulent friction
 430 (flows with $\mu = 0.01$ – 0.02) or by (ii) the Coulomb friction (flows with $\mu = 0.05$). Note that Figure
 431 6 also shows that the total friction S increases with a larger μ . Nevertheless, the output of the
 432 simulation (velocity and flow depth) is similar regardless of which μ - ξ pair variant is chosen.
 433



434
 435 Figure 6: Values of Coulomb friction, turbulent friction, and total friction S as a function of the selected Coulomb
 436 friction coefficient μ . The plotted values are averages of the friction magnitudes of all best-fit simulations. The blue
 437 line represents the Coulomb friction contribution. The red line is the turbulent friction, and the yellow line is the total
 438 friction.
 439

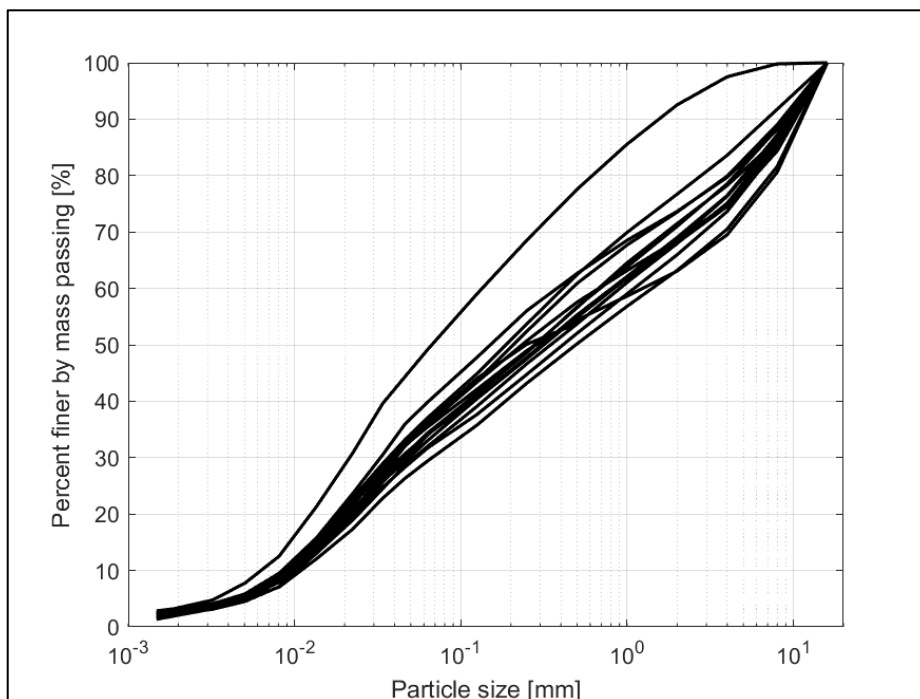
440 4.3 Grain size distribution

441 Samples from 14 debris flows were analyzed for their grain size distribution (Figure 7 and
 442 Appendix G). Note that there was a sediment sample but no monitoring data for the event on
 443 the 4th of October 2021. All events show a very similar grain size distribution. An exception,
 444 and thus an outlier, is a sediment sample that has a larger relative abundance of fine-grained
 445 material. This sample was taken from a debris flow, which occurred on the 2nd of July 2019.
 446 For all samples, the clay fraction has a relative mass abundance of 2–3%, the silt fraction 27–

447 35%, the sand fraction 27–40% and the part of the gravel fraction that is covered by the
448 analysis 23–37%. Note that the gravel fraction >16 mm was also analyzed (Appendix G). Yet
449 we normalized the grain size data to 16 mm, because it was not feasible to collect larger mass-
450 representative samples. Therefore, we acknowledge that the upper percentiles are affected
451 and thus biased by this cut-off and the related percentage values have to be considered with
452 caution.

453 For all samples, we measured grain sizes of 0.015–0.02 mm for the 16% percentile, 4–9 mm
454 for the 84% percentile and 10–15 mm for the 95% percentile. The median grain size ranges
455 from 0.15 mm to 0.5 mm. In general, the material was very poorly sorted with a skewness
456 towards the fine-grained fraction. Interestingly, the grain size distribution was quite similar
457 for all sampled material. Based on the available datasets, we are neither able to determine
458 whether the mean grain size is more variable in space than in time, nor can we detect whether
459 the coarse-grained fraction (>16 mm) could be highly variable whereas the fine-grained
460 material is more homogeneous. However, similar to the mineralogical composition, which is
461 also quite similar between the various flows, we interpret that the rather homogeneous
462 granulometric composition at least of the fine-grained portion of the sediment is the direct
463 consequence of the cascade of sediment mixing in the upstream part of the Illgraben
464 (Schlunegger et al., 2009).

465



466

467 Figure 7: Diagram showing the grain size distribution of all 14 sampled debris flow deposits, truncated at a
468 maximum grain size of 16 mm.

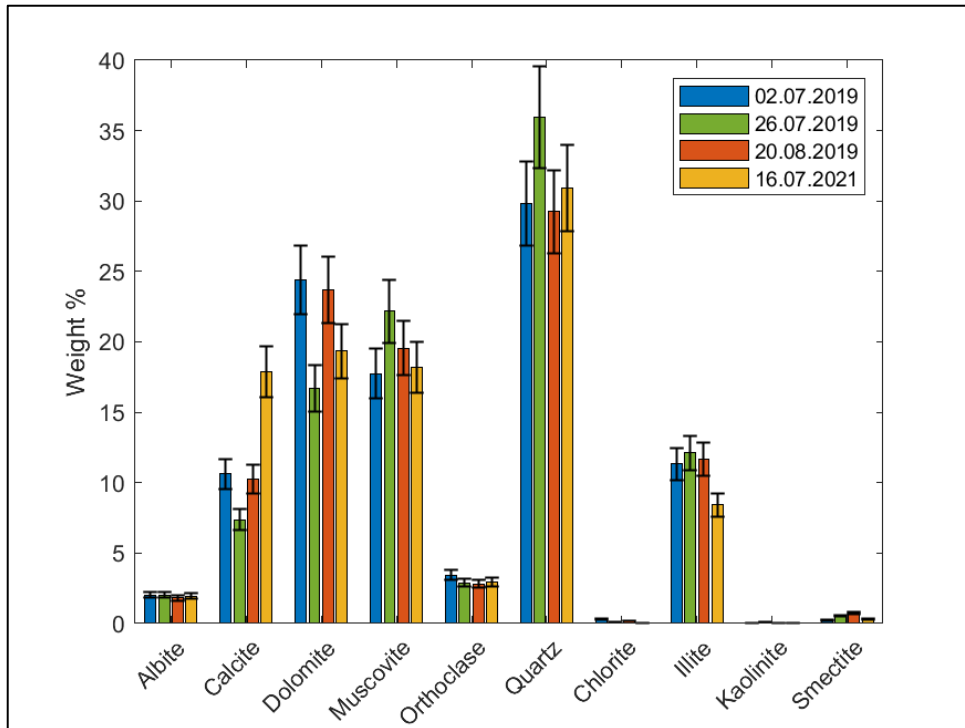
469

470 4.4 Powder XRD

471 The results of the powder XRD analysis (Appendix H) show that quartz was the main mineral
472 of the silt fraction and contributes between 29 and 36 wt% (Figure 8). In addition, dolomite
473 (17–24 wt%), muscovite (18–22 wt%), calcite (7–18 wt%) and illite minerals (8–12 wt%) are
474 present in all samples. Feldspar grains occur by < 5 wt%, and the clay minerals chlorite,
475 kaolinite and smectite are present in small quantities (< 1%) or are below the detection limit.
476 Calcite shows the greatest variation in the mineralogical composition with differences up to 11
477 wt%. The other main components including quartz, dolomite, muscovite and illite show
478 variations with a maximum of 7 wt%. The feldspar minerals albite and orthoclase are very
479 homogeneously distributed in the four samples. Overall, the variations in the mineralogical
480 composition between the different samples are only minor and often lie within the
481 methodological error of $\pm 10\%$ of the measured values. Yet, some albeit minor differences can
482 be detected when the compositions of the coarse- and fine-grained samples are compared.
483 In the coarse-grained sample, calcite crystals are more abundant than in the sample
484 characterizing a fine-grained debris flow. In contrast, the latter sample has a larger relative
485 abundance of illite minerals than the sample made up of coarser sediments. Although the
486 database is sparse, we tentatively consider these differences to reflect a source signal where
487 the heavily fractured basement rocks and Triassic schists, which also host the illite crystals,
488 have the potential to supply larger volumes of fine-grained material than the bedrock made up
489 of limestones.

490 From the clay minerals, only smectite can absorb larger amounts of water (Likos and Lu,
491 2002). However, the x-ray spectra of muscovite and smectite crystals cannot be distinguished
492 with the applied XRD method. Because the basement rocks and the Triassic schists are
493 considered to be the source of the clay minerals in the catchment area (Schlunegger et al.,
494 2009), the signal is more likely related to the fine-grained muscovite (sericite) than to the
495 smectite minerals (Scheiber et al., 2013). Therefore, swelling clay minerals are expected to
496 be of minor importance in this case.

497

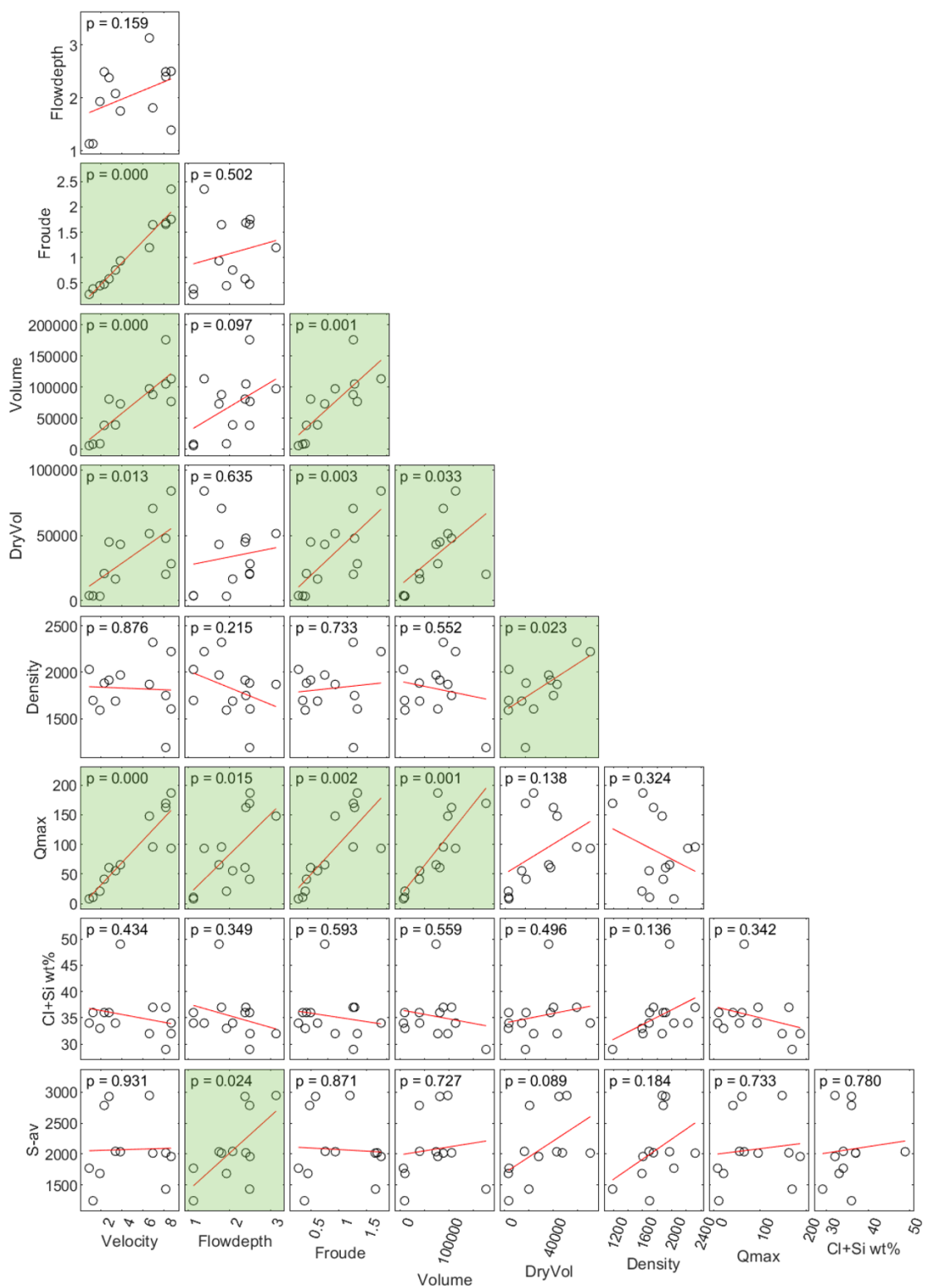


498

499 Figure 8: Mineralogical composition of four samples analyzed by powder-XRD. The black error bars indicate a
 500 methodological error of 10% of the measured value. The material representing the flow on the 2nd of July 2019 was
 501 exceptionally fine-grained (Appendix G); the flow on the 26th of July of the same year was an event with a high
 502 velocity (8.69 m/s), and it was the most rapid flow (Table 1). The debris flow on the 20th of August, again in 2019,
 503 was very slow (0.89 m/s) and it was indeed the slowest flow during the survey period (Table 1). The material taken
 504 from the debris flow on the 16th of July 2021 was characterized by a rather coarse-grained matrix (Appendix G).
 505

506 4.5 Statistical evaluation of the debris flow properties

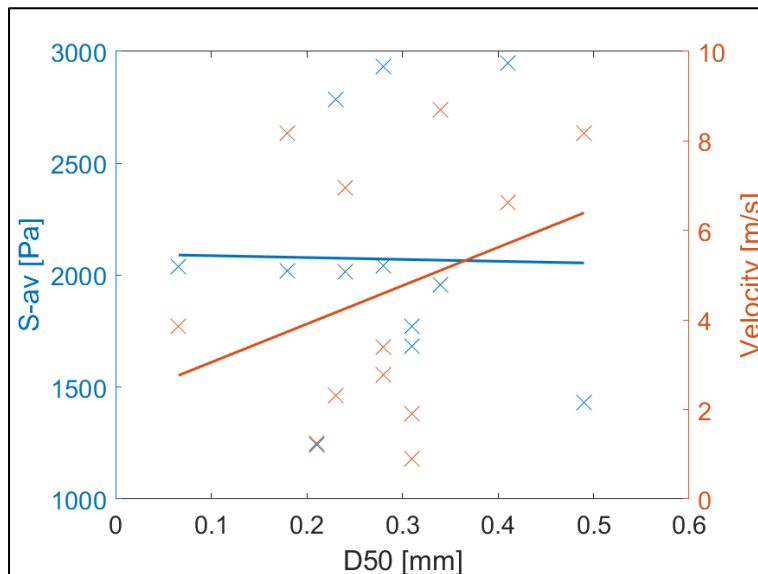
507 A statistical evaluation of the debris flow parameters measured at the monitoring station shows
 508 a positive correlation between velocity, flow depth, volume, and maximum discharge (Figure
 509 9). While velocity, volume, and maximum discharge correlate very strongly among themselves
 510 as they are physically related (auto-correlation), the correlation of these parameters with the
 511 flow depth is less evident, yet a weak positive correlation is certainly visible. Accordingly, and
 512 as expected (McArdell et al., 2003), a debris flow with a large volume tends to have a large
 513 flow velocity and flow depth, which consequently also results in a large maximum discharge
 514 and a large Froude number. On the other hand, debris flows that have a small volume are
 515 also slow, and they have both a small flow depth and a low Froude number. Interestingly, clear
 516 correlations between grain size, clay content and flow properties are not visible in our analyses
 517 (Figure 10). Also, no correlation between the inferred water content and the volume or
 518 maximum discharge was found for these events. Yet, the total friction values that are extracted
 519 from the modelling results tend to show a positive correlation with the flow depth, and a weak
 520 positive correlation with the density and thus the water content (Figure 9).



521
522
523
524
525
526

Figure 9: Statistical correlations between dynamic properties of the debris flows with a statistical p-value. For correlation tests a significance level of 0.05 is considered. Correlations with p-values < 0.05 can therefore be considered as significant (illustrated with green color). Measurements from the monitoring station at the Illgraben and values derived from them are front velocity [m/s], maximum flow depth [m], Froude number [], total volume [m³], dry sediment volume [m³], density of a flow [kg/m³], which points to the water content and the maximum

527 discharge [m^3/s]. From the grain size analyses, we have the percentage of the sum of clay and silt in the sample
 528 [wt%]. From the modelling with RAMMS we get the total amount of friction [Pa] as average of all best-fit simulations
 529 of a certain event. The plots were generated using a modified version of the Correlation Matrix Scatterplot by Chow
 530 (2022) for MATLAB. Note that a statistical p-value with $p = 0.000$ means that the value is less than 0.0005, and
 531 therefore it is rounded down to 0.
 532



533
 534 Figure 10: Correlation (first order polynomial trendlines accomplished by least square fitting) between the total
 535 amount of friction S-av as average of all best-fit simulations of a certain event and the D50 value of the
 536 corresponding sediment sample (blue), and correlation between the measured velocity of the flow and the D50
 537 value of the corresponding sediment sample (red).
 538

539 **5 Discussion**

540 The debris flows observed in the years 2019, 2021 and 2022 show large differences in their
 541 dynamics, where flow depths and flow velocities varied by a factor of 3 and 10, respectively.
 542 Despite these variabilities in the surveyed parameters, most of the flows could be simulated
 543 with RAMMS, and the model outputs yielded consistent results regarding the underlying
 544 controls and the simulated flow kinematics and properties (see Appendix C, D, E and F, and
 545 the related z-values). In the following section, we discuss how the various parameters such
 546 as the grain size and mineralogical distribution of the fined-grained matrix as well as the friction
 547 properties potentially exerted a control on the surveyed debris flows.
 548

549 *5.1 Relationships between volume, flow velocity and flow depth, and controls on friction*
 550 *properties*

551 The statistical tests show positive correlations between volume, flow velocity, flow depth and
 552 maximum discharge rate. Our results are thus consistent with similar results reported by
 553 Rickenmann (1999), de Haas et al. (2015) and Hürlimann et al. (2015) and reflect the open-
 554 channel hydraulic principles used to compute these parameters (McArdell et al., 2023).
 555 Indeed, as shown by the aforementioned authors, flows with larger volumes may contain a
 556 larger number of pebbles and boulders, which according to Johnson et al. (2012) are likely to

557 accumulate on the front of these flows. As a result, the frictional resistance of the frontal part
558 increases (Iverson, 1997), with the consequence of a damming effect such as that the flow
559 depths will increase. We indeed see such a mechanism at work in the surveyed flows through
560 positive correlations between flow depth, flow velocity and flow volume. We thus infer that the
561 volume can be considered as the most important driving parameter for explaining the debris
562 flow dynamics in the Illgraben system and therefore can be considered as a key parameter.
563 This confirms standard practice in hazard analysis, which gives primary importance to event
564 volume. We note that this argument relies on the debris flows all having the same initial grain
565 size distribution, which, as discussed above, we can only document for sediment sizes smaller
566 than 16 mm. Yet, we acknowledge that a visual comparison of the videos (Appendix B) clearly
567 shows differences in the abundance of relatively coarse sediment (e.g., boulders). A more
568 detailed analysis on this topic will require additional data and is beyond the scope of this paper.
569 The evaluation of the RAMMS simulations shows that there are several μ - ξ pairs, which yield
570 ideal solutions upon simulating the surveyed debris flows. In particular, the same flow can
571 successfully be reproduced by RAMMS with large and low Voellmy μ -values. However, an
572 assessment of which of these possibilities is more appropriate can be found if the flow velocity
573 is used as a criterion. Indeed, our analysis showed that debris flows with a high velocity (up
574 to 6-7 m/s) tend to be dominated by a large Coulomb friction (large μ -value), whereas flows
575 with a low velocity have a low Coulomb friction (low μ -value) but a relatively high turbulent
576 friction (Figure 5). Yet for flows with velocities that are larger than 6-7 m/s, these relatively
577 simple relationships break down most likely because such flows appear to be in a condition
578 where the flow pattern is more complex (e.g., roll waves with Froude numbers that are much
579 larger than 1 to 1.5, Table 1).

580 We note that while it is tempting to interpret such low- μ flows as being 'laminar' and large- μ
581 flows as 'turbulent' (because of the low and high Froude numbers, see also Figure 5),
582 independent criteria for determining the presence or absence of turbulence in debris flows are
583 not yet available. A hydraulics-based estimate based on the Reynolds number to characterize
584 the presence or absence of turbulence (e.g. Henderson, 1966) requires estimates of the
585 rheology of the entire flow, which are not available. In addition, it is unclear to what extent
586 rheological measurements of fine sediment slurries can represent the overall viscosity of the
587 flow given the presence of other processes such as the jamming of particles in the flow
588 (Kostynic et al., 2022). Yet, such calculations are beyond the scope of this contribution.

589

590 *5.2 Influence of the grain size distribution and mineralogy*

591 The granulometric analysis of the levee deposits indicates a rather homogeneous grain size
592 distribution for the clay, silt, sand and the fine-grained gravel fraction. The grain size
593 distribution fits quite well with the granulometric analyses of the debris flow deposits at the

594 Illgraben published by Hürlimann et al. (2003). Because of a lack of correlations between the
595 relative proportion of the fine fraction to the parameters that characterize the flow properties
596 (e.g., friction and flow velocity; Figure 10), the variations in the dynamics of these flows cannot
597 be simply explained by a simple fixed friction relation such as in the Voellmy relation. This
598 inference is consistent with the notion by Iverson (2003) who states that the evolution of debris
599 flow behavior upstream of the front is likely to be complex. In the same sense, because of the
600 homogeneity of the samples with respect to the grain size distribution of the components
601 smaller than 16 mm, also the relative abundance of the sand to the fine-grained gravel fraction
602 cannot be related to variations in the flow dynamics. Nevertheless, an influence of the grain
603 size composition on the debris flow dynamics, as described by de Haas et al. (2015) and
604 Hürlimann et al. (2015), cannot be fully excluded (see section 1.1). Because the relative
605 abundances of the different fractions are similar, their potential influence on the flow properties
606 should also be similar for each event. Due to this similarity, such relationships (if present)
607 would not be detectable with the measurements presented herein. Admittedly, we also have
608 no information to exclude a potential control of the coarse-grained fraction such as coarse
609 gravel, cobbles, and boulders, on the flow dynamics, as described by de Haas et al. (2015).
610 Attempts to reconstruct the full grain size distribution are hampered by a lack of information
611 on the grain size below the surface of the flow (e.g., Uchida et al., 2021). In addition, the
612 influence of small changes of the topography on the results was not investigated here, but
613 could improve the correlations of the flow properties to grain size if adequately considered.
614 Similar to the grain size distribution of the fine-grained matrix, we do not see a relationship
615 between the mineralogical composition of the matrix and the flow properties. Among the
616 various minerals that are present in the debris flow deposits (Appendix H), we expect to see
617 a control of the sheet silicates on the velocity of the flows, mainly because clay minerals and
618 particularly smectite-type of clays have the potential to absorb water in their crystal structure
619 (see section 1.1). We therefore expect that a high relative abundance of such minerals will
620 alter the flow rheology and particularly the flows' turbulent friction, which is expected to impact
621 the flow velocity. Apparently, this is not the case at the Illgraben. We consider this absence of
622 relationships to reflect a supply signal, because the relative abundance of swelling minerals
623 is negligible in the source area where other sheet silicates such as illite and muscovite crystals
624 predominate (Scheiber et al., 2013). These silicates don't have swelling properties and
625 apparently do not impact the velocity of the debris flows at the Illgraben. However, the
626 homogeneity in terms of the mineral composition and also the grain size composition between
627 the samples confirms the results of previous studies that inferred the occurrence of an efficient
628 mixing mechanism as the material is transferred from the source area to the Rhone River
629 (Schlunegger et al., 2009; Berger et al., 2011a).

630

631 **Conclusion**

632 The results obtained in the Illgraben system by comparing various debris flow parameters with
633 data from runout modelling, grain size analyses, XRD analyses can be summarized as follows:

- 634 1) The simulation of debris flows with RAMMS yields multiple solutions with different friction
635 coefficients μ and ξ in the Voellmy equation. The resulting Coulomb and turbulent friction
636 are correlated with the Froude number and runout velocity of the debris flow yet only as
637 long as the flow velocity is $< 6-7$ m/s.
- 638 2) The dynamics of a debris flow in the Illgraben (i.e., flow velocity and flow depth) is strongly
639 dependent on its volume. If information about the sediment volume in the source area is
640 available, the parameters for simulating a potentially worst-case debris flow and its impact
641 can theoretically be assessed with some uncertainties.
- 642 3) Due to the relatively large homogeneity of the deposits with respect to the grain size
643 distribution and the mineralogical composition, an efficient mixing process in the Illgraben
644 can be inferred.
- 645 4) Based on these data, variations in the dynamics of different debris flows cannot be
646 attributed to the grain size distributions of the clay, silt, sand or fine-grained gravel
647 fractions. Consequently, an assessment of a potential debris flow or a definition of a
648 simulation based on grain size compositions in the source area is not possible in the case
649 presented here.

650 Such relationships are particularly useful for the assessment of natural hazards, as they
651 provide specific evidence for the estimation of a debris flow and its impact.

652

653 **Acknowledgement**

654 We are grateful for the technical support provided by Franziska Nyffenegger (grain size
655 analysis), Pierre Lanari and Michael Schwenk (statistics) as well as Frank Gfeller and
656 Anulekha Prasad (XRD analysis). We thank the WSL staff for their support with sampling and
657 the support of Marc Christen and Perry Bartelt (RAMMS) is greatly appreciated.

658

659 **Data availability**

660 All data used in this paper are listed in Table 1 and in the supplementary files.

661

662 **Author contributions**

663 BM and FS designed the study. DB conducted the experiments, collected the data and
664 processed the samples. DB wrote the paper, with contributions by FS and BM. All authors
665 discussed the article.

666

667 **Competing interests**

668 The authors declare that they have no conflict of interest.

669

670 **References**

671 Abraham, M.T., Satyam, N., Peddholla Reddy, S.K., and Pradhan, B.: Runout modeling and
672 calibration of friction parameters of Kurichermala debris flow, India. *Landslides*, 18, 737–
673 754. <https://doi.org/10.1007/s10346-020-01540-1>.

674 Allen, P. A.: *Earth surface processes*. Blackwell Science, 1997.

675 Badoux, A., Graf, C., Rhyner, J., Kuntner, R., and McArdell, B. W.: A debris-flow alarm system
676 for the Alpine Illgraben catchment: Design and performance, *Nat. Hazards*, 49, 517–
677 539, 2007. <https://doi.org/10.1007/S11069-008-9303-X/FIGURES/7>

678 Barshad, I.: Absorptive and swelling properties of clay-water system, *Clays Clay Miner.*, 1(1),
679 70–77, 1952.

680 Bartelt, P., Valero, C. V., Feistl, T., Christen, M., Bühler, Y., and Buser, O.: Modelling cohesion
681 in snow avalanche flow, *J. Glaciol.*, 61, 837–850, 2015.
682 <https://doi.org/10.3189/2015JoG14J126>

683 Belli, G., Walter, F., McArdell, B., Gheri, D., and Marchetti, E.: Infrasonic and Seismic Analysis
684 of Debris-Flow Events at Illgraben (Switzerland): Relating Signal Features to Flow
685 Parameters and to the Seismo-Acoustic Source Mechanism, *J. Geophys. Res. Earth*,
686 127, e2021JF006576, 2022. <https://doi.org/10.1029/2021JF006576>

687 Bennett, G. L., Molnar, P., McArdell, B. W., Schlunegger, F., and Burlando, P.: Patterns and
688 controls of sediment production, transfer and yield in the Illgraben, *Geomorphology*, 188,
689 68–82, 2013. <https://doi.org/10.1016/j.geomorph.2012.11.029>

690 Berger, C., Christen, M., Speerli, J., Lauber, G., Ulrich, M., And McArdell, B. W.: A comparison
691 of physical and computer-based debris flow modelling of a deflection structure at
692 Illgraben, Switzerland, *Data Acquisition and Modelling (Monitoring, Processes,*
693 *Technologies, Models)*, 212–220, 2016.

694 Berger, C., McArdell, B. W., Fritschi, B., and Schlunegger, F.: A novel method for measuring
695 the timing of bed erosion during debris flows and floods, *Water Res. Res.*, 46, 2010.
696 <https://doi.org/10.1029/2009WR007993>

697 Berger, C., McArdell, B. W., & Schlunegger, F.: Sediment transfer patterns at the Illgraben
698 catchment, Switzerland: Implications for the time scales of debris flow activities,
699 *Geomorphology*, 125, 2011a. 421–432.
700 <https://doi.org/10.1016/j.geomorph.2010.10.019>

701 Berger, C., McArdell, B. W., and Schlunegger, F.: Direct measurement of channel erosion by
702 debris flows, Illgraben, Switzerland, *J. Geophys. Res.*, 116, 2011b.
703 <https://doi.org/10.1029/2010JF001722>

704 Bumann, N.: Effect of Geological Preconditioning on Sediment Production in the Illgraben
705 Catchment [Ms thesis]. University of Bern, 2022.

706 Chatterji, P.K., and Morgestern, N.R., 1990. A modified shear strength formulation for swelling
707 clay soils. In: Proc. Symp. Physico-Chemical Aspects of Soil, Rock and Related
708 Materials, St. Louis. ASTM Spec. Tech. Publ. N1095, 118-139.

709 Choi, C. E., Ng, C. W. W., Au-Yeung, S. C. H., and Goodwin, G. R.: Froude characteristics of
710 both dense granular and water flows in flume modelling, *Landslides*, 12, 1197–1206,
711 2015. <https://doi.org/10.1007/S10346-015-0628-8/FIGURES/11>

712 Chow, J. : Correlation Matrix Scatterplot, 2022.
713 [https://www.mathworks.com/matlabcentral/fileexchange/53043-correlation-matrix-](https://www.mathworks.com/matlabcentral/fileexchange/53043-correlation-matrix-scatterplot)
714 [scatterplot](https://www.mathworks.com/matlabcentral/fileexchange/53043-correlation-matrix-scatterplot)

715 Christen, M., Bühler, Y., Bartelt, P., Leine, R., Glover, J., Schweizer, A., Graf, C., McArdell, B.
716 W., Gerber, W., Deubelbeiss, Y., Feistl, T., and Volkwein, A.: Integral hazard
717 management using a unified software environment numerical simulation tool “RAMMS”
718 for gravitational natural hazards, 2012. www.interpraevent.at

719 Church, M., McLean, D., and Wolcott, J.: River bed gravels : sampling and analysis, *Sediment*
720 *Transport in Gravel-Bed Rivers*, 43–88, 1987.
721 <https://cir.nii.ac.jp/crid/1572261549037050368.bib?lang=en>

722 Coelho, A. A.: TOPAS and TOPAS-Academic: An optimization program integrating computer
723 algebra and crystallographic objects written in C++, *J. Applied Crystall.*, 51, 210–218,
724 2018. <https://doi.org/10.1107/S1600576718000183>

725 de Haas, T., Braat, L., Leuven, J. R. F. W., Lokhorst, I. R., and Kleinhans, M. G.: Effects of
726 debris flow composition on runout, depositional mechanisms, and deposit morphology
727 in laboratory experiments, *J. Geophys. Res. Earth Surface*, 120, 1949–1972, 2015.
728 <https://doi.org/10.1002/2015JF003525>

729 de Haas, T., McArdell, B. W., Nijland, W., Åberg, A. S., Hirschberg, J., and Huguenin, P.: Flow
730 and Bed Conditions Jointly Control Debris-Flow Erosion and Bulking. *Geophys. Res.*
731 *Lett.*, 49, e2021GL097611, 2022. <https://doi.org/10.1029/2021GL097611>

732 Deubelbeiss, Y., and Graf, C.: Two different starting conditions in numerical debris-flow
733 models - Case study at Dorfbach, Randa (Valais, Switzerland). *Jahrestagung Der*
734 *Schweizerischen Geomorphologischen Gesellschaft*, 2011.

735 Di Maio, C.: Exposure of bentonite to salt solution: osmotic and mechanical effects.
736 *Géotechnique XLVI* (4), 695–707, 1996.

737 Di Maio, C., Santoli, L., and Schiavone, P.: Volume change behaviour of clays: the influence
738 of mineral composition, pore fluid composition and stress state. *Mechanics Mat.*, 36,
739 435-451, 2004. [https://doi.org/19.1016/S0167-6636\(03\)00070-X](https://doi.org/19.1016/S0167-6636(03)00070-X)

740 Frank, F., McArdell, B. W., Huggel, C., and Vieli, A.: The importance of entrainment and
741 bulking on debris flow runout modeling: examples from the Swiss Alps, *Nat. Hazards*
742 *Earth Sys. Sci.*, 15, 2569-2583, 2015, <https://doi.org/10.5194/nhess-15-2569-2015>;

743 Frank, F., McArdell, B. W., Oggier, N., Baer, P., Christen, M., and Vieli, A.: Debris-flow
744 modeling at Meretschibach and Bondasca catchments, Switzerland: sensitivity testing
745 of field-data-based entrainment model, *Nat. Hazards Earth Sys. Sci.*, 17, 801-815, 2017.
746 <https://doi.org/10.5194/nhess-17-801-2017>

747 Gabus, J. H., Weidmann, M., Sartori, M., and Burri M.: Blatt 1287 Sierrre - Geologischer Atlas
748 der Schweiz 1:25 000, Erläuterungen, Bundesamt für Landestopografie swisstopo,
749 2008.

750 Henderson, F.M.: *Open Channel flow*. New York, MacMililan, 1966.

751 Hirschberg, J., Badoux, A., McArdell, B. W., Leonarduzzi, E., and Molnar, P.: Evaluating
752 methods for debris-flow prediction based on rainfall in an Alpine catchment, *Nat.*
753 *Hazards Earth Sys. Sci.*, 21, 2773–2789, 2021. [https://doi.org/10.5194/NHESS-21-](https://doi.org/10.5194/NHESS-21-2773-2021)
754 [2773-2021](https://doi.org/10.5194/NHESS-21-2773-2021)

755 Hirschberg, J., Fatichi, S., Bennett, G. L., McArdell, B. W., Peleg, N., Lane, S. N., Schlunegger,
756 F., and Molnar, P.: Climate Change Impacts on Sediment Yield and Debris-Flow Activity
757 in an Alpine Catchment, *J. Geophys. Res. Earth Surface*, 126, e2020JF005739, 2021.
758 <https://doi.org/10.1029/2020JF005739>

759 Hirschberg, J., McArdell, B. W., Badoux, A., and Molnar, P.: Analysis of rainfall and runoff for
760 debris flows at the Illgraben catchment, Switzerland. *Debris-Flow Hazards Mitigation:*
761 *Mechanics, Monitoring, Modeling, and Assessment - Proceedings of the 7th*
762 *International Conference on Debris-Flow Hazards Mitigation*, 693–700, 2019.

763 Hübl, J., Suda, J., Proske, D., Kaitna, R., and Scheidl, C.: Debris Flow Impact Estimation,
764 *International Symposium on Water Management and Hydraulic Engineering*, 137–148,
765 2009. <https://www.researchgate.net/publication/258550978>

766 Hürlimann, M., McArdell, B. W., and Rickli, C.: Field and laboratory analysis of the runout
767 characteristics of hillslope debris flows in Switzerland, *Geomorphology*, 232, 20–32,
768 2015. <https://doi.org/10.1016/J.GEOMORPH.2014.11.030>

769 Hürlimann, M., Rickenmann, D., and Graf, C.: Field and monitoring data of debris-flow events
770 in the Swiss Alps, *Can. Geotech. J.*, 40, 161–175, 2003. <https://doi.org/10.1139/t02-087>

771 Iverson, R. M.: The physics of debris flows, *Rev. Geophys.*, 35, 245–296, 1997.
772 <https://doi.org/10.1029/97RG00426>

773 Jianjun, Z., Zhang, Y.X.: Numerical simulation of debris flow runout using Ramms: a case
774 study of Luzhuang Gully in China. *Computer modeling in Engineering & Science*, 121,
775 981-1009. <https://doi.org/10.32604/cmes.2019.07337>.

776 Johnson, C. G., Kokelaar, B. P., Iverson, R. M., Logan, M., Lahusen, R. G., and Gray, J. M.
777 N. T.: Grain-size segregation and levee formation in geophysical mass flows, *J.*
778 *Geophys. Res. Earth Surface*, 117, 2012. <https://doi.org/10.1029/2011JF002185>
779 Kaitna, R., Palucis, M. C., Yohannes, B., Hill, K. M., and Dietrich, W. E.: Effects of coarse
780 grain size distribution and fine particle content on pore fluid pressure and shear behavior
781 in experimental debris flows, *J. Geophys. Res. Earth Surf.*, 121, 415–441, 2016.
782 doi:10.1002/2015JF003725.

783 Likos, W. J., and Lu, N.: Water vapor sorption behavior of smectite-kaolinite mixtures. *Clays*
784 *Clay Mineral*, 50, 553–561, 2002.
785 <https://doi.org/10.1346/000986002320679297/METRICS>

786 McArdell, B. W., Bartelt, P., and Kowalski, J.: Field observations of basal forces and fluid pore
787 pressure in a debris flow, *Geophys. Res. Lett.*, 34, 2007.
788 <https://doi.org/10.1029/2006GL029183>

789 McArdell, B. W., and Sartori, M.: The Illgraben torrent system. In E. Reynard (Ed.), *World*
790 *geomorphological landscapes, Landscapes and landforms of Switzerland* (pp. 367-378),
791 2021. https://doi.org/10.1007/978-3-030-43203-4_25.

792 McArdell, B. W.: Field measurements of forces in debris flows at the Illgraben: implications for
793 channel-bed erosion. *Int. J. Erosion Control Eng.*, 9, 194-198, 2016.
794 <https://doi.org/10.13101/ijece.9.194>

795 McArdell, B. W., Hirschberg, J., Graf, C., Boss, S., and Badoux, A.: Illgraben debris-flow
796 characteristics 2019-2022. *EnviDat*. 2023. <https://www.doi.org/10.16904/envidat.378>.

797 Medina, V., Hürlimann, M. and Bateman, A.: Application of FLATModel, a 2D finite volume
798 code, to debris flows in the northeastern part of the Iberian Peninsula. *Landslides* 5,
799 127–142, 2008. <https://doi.org/10.1007/s10346-007-0102-3>

800 Mikoš, M., and Bezak, N.: Debris flow modelling using RAMMS model in the Alpine
801 environment with focus on the model parameters and main characteristics. *Front. Earth*
802 *Sci.*, 8 – 2020, 2021. <https://doi.org/10.3389/feart.2020.605061>.

803 Naef, D., Rickenmann, D., Rutschmann, P., and McArdell, B. W.: Comparison of flow
804 resistance relations for debris flows using a one-dimensional finite element simulation
805 model, *Nat. Hazards Earth Sys. Sci.*, 6, 155–165, 2006. [www.nat-hazards-earth-syst-](http://www.nat-hazards-earth-syst-sci.net/6/155/2006/)
806 [sci.net/6/155/2006/](http://www.nat-hazards-earth-syst-sci.net/6/155/2006/)

807 Pierson, T. C.: Flow behavior of channelized debris flows, Mount St. Helens, Washington. In
808 A. Abrahams (Ed.), *Hillslope Processes* (pp. 269–296), 1986.

809 Rickenmann, D.: Empirical Relationships for Debris Flows, *Nat. Hazards*, 19, 47–77, 1999.

810 Rietveld, H. M.: A profile refinement method for nuclear and magnetic structures, *J. Applied*
811 *Crystallography* 2, 65–71, 1969. <https://doi.org/10.1107/S0021889869006558>

812 Salm, B.: Flow, flow transition and runout distances of flowing avalanches, *Annal. Glaciol.* 18,
813 221–226, 1993. <https://doi.org/10.3189/S0260305500011551>

814 Salm, B., Burkard, A., and Gubler, H. U.: Berechnung von Fliesslawinen. Eine Anleitung fuer
815 Praktiker mit Beispielen, In *Mitteilungen des Eidg. Institutes für Schnee- und*
816 *Lawinenforschung* (Vol. 47), 1990.

817 Scheiber, T., Pfiffner, O.A., and Schreurs, G.: Upper crustal deformation in continent-continent
818 collision: A case study from the Bernhard nappe complex (Valais, Switzerland).
819 *Tectonics*, 32, 1320-1342, 2013. <https://doi.org/10.1002/tect.20080>.

820 Schlunegger, F., Badoux, A., McArdell, B. W., Gwerder, C., Schnydrig, D., Rieke-Zapp, D.,
821 and Molnar, P.: Limits of sediment transfer in an alpine debris-flow catchment, Illgraben,
822 Switzerland, *Quat. Sci. Rev.*, 28, 1097–1105, 2009.
823 <https://doi.org/10.1016/j.quascirev.2008.10.025>

824 Schlunegger, F., Garefalakis, P.: Einführung in die Sedimentologie. Schweizerbart, Stuttgart,
825 305 p., 2023.

826 Schürch, P., Densmore, A. L., Rosser, N. J., and McArdell, B. W.: Dynamic controls on erosion
827 and deposition on debris-flow fans, *Geology*, 39, 827–830, 2011.
828 <https://doi.org/10.1130/G32103.1>

829 Simoni, A., Mammoliti, M., and Graf, C.: Performance Of 2D debris flow simulation model
830 RAMMS. *Ann. Int. conf. GEOS*, 2012. https://doi.org/10.5176/2251-3361_GEOS12.59

831 Swisstopo: Bundesamt für Landestopografie, 2022.
832 <https://www.swisstopo.admin.ch/de/geodata.html>

833 Uchida, T., Nishiguchi, Y., McArdell, B. W., and Satofuka, Y.: The role of the phase shift of
834 fine particles on debris flow behavior: a numerical simulation for a debris flow in
835 Illgraben, Switzerland, *Can. Geotech. J.*, 58, 23-34, 2021. [https://doi.org/10.1139/cgj-](https://doi.org/10.1139/cgj-2019-0452)
836 [2019-0452](https://doi.org/10.1139/cgj-2019-0452)

837 Voellmy, A.: Über die Zerstörungskraft von Lawinen, *Schweiz. Bauzeitschrift*, 73, 212–217,
838 1995. <https://doi.org/10.5169/seals-61891>

839 WSL. RAMMS::DEBRISFLOW User Manual v1.8.0 (v1.8.0). WSL, 2022.
840 <https://ramms.slf.ch/en/modules/debrisflow.html>

841

842

Appendix A: Measurements from monitoring station at the Illgraben

Event start	Front velocity CD 28-29 (m/s)	Max flow depth laser (m)	Max flow depth radar (m)	Mean bulk density laser (kg/m ³)	Peak velocity (quantile 0.99) laser CD 28-29 (m/s)	Peak velocity (quantile 0.99) radar CD 28-29 (m/s)	Peak discharge (quantile 0.99) laser CD 28-29 (m/s)	Volume laser CD 28-29 (m ³)	Flow duration (min)
21.06.2019 21:44	6.62	3.13	2.69	1870	6.55	6.57	147.61	97394	43
02.07.2019 01:26	3.86	1.75	1.73	1971	5.78	5.38	65.58	73188	52
26.07.2019 19:46	8.69	1.39	1.41	2223	9.74	9.98	93.26	113310	65
11.08.2019 19:07	6.95	1.81	1.89	2323	6.90	6.91	95.63	88064	88
20.08.2019 19:03	0.89	1.13	1.10	2031	1.36	1.36	8.06	6137	37
24.06.2021 17:11	8.18	2.40	2.49	1750	8.16	8.10	162.20	105032	38
06.07.2021 20:43	8.69	2.50	2.58	1605	8.65	8.67	186.61	76906	28
16.07.2021 05:43	2.78	2.38	2.44	1916	3.22	3.30	60.70	80879	77
07.08.2021 16:22	2.32	2.49	2.17	1884	2.89	2.74	41.19	38737	46
19.09.2021 08:57	1.25	1.13	1.22	1697	1.41	1.39	10.67	8538	43
05.06.2022 12:33	3.39	2.08	2.15	1690	4.14	4.32	55.42	39498	55
04.07.2022 22:54	8.18	2.49	2.60	1189	8.46	7.36	169.14	175929	39
08.09.2022 02:06	1.91	1.93	1.77	1592	1.85	1.87	20.94	9283	20

Appendix B: Video recordings of debris flows. The video camera is placed at the Survey Station (see Figure 1c in main text)



Appendix C: Exemplary evaluation of the simulations of the debris flow event on 24.06.2021

Input data composed of raster and shape files, simulation settings and measurements from the monitoring station.

Event	24.06.2021
DTM	DTM_0.5.tif
DTM resolution [m]	0.5
calculation domain	calcdom.shp
release area	hydrograph.shp
stop parameter [%]	5
sim resolution [m]	0.5
end time [s]	600
dump step [s]	2
erosion layer	erosion.shp
erosion density [kg/m ³]	2000
erosion rate [m/s]	0.025
pot. Erosion depth [per kPa]	0.1
critical shear stress [kPa]	1
max erosion depth [m]	1
density [kg/m ³]	1750
inflow direction [°]	60
vol [m ³]	105032
Qmax [m ³ /s]	162.2
t1 [s]	10
v [m/s]	8.18
Front velocity CD 28-29 (m/s)	8.18
Max flow depth laser (m)	2.4
Max flow depth radar (m)	2.49
Peak velocity (quantile 0.99) laser CD 28-29 (m/s)	8.16
Peak velocity (quantile 0.99) radar CD 28-29 (m/s)	8.1
Flow duration (min)	38
CD28-CD29	134m
CD27-CD29	460m
Froude number	1.69

Output data with velocity (v) and flow depth (av_maxd_P). These variables were compared with the results of the field survey to determine the best-fit simulation (green) for each μ . The z-values are calculated from the laser measurement (Max flow depth laser, see above).

Simulation	μ []	ξ [m/s ²]	v [m/s]	maxd_P1 [m]	maxd_P2 [m]	maxd_P3 [m]	maxd_P4 [m]	av_maxd_P [m]	Froude number []	Qmax [m ³ /s]	z value laser	z value radar
1	0.02	1400	8.9	1.99	2.30	2.54	2.93	2.44	1.82	140	0.09	0.09
2	0.02	800	7.9	3.00	2.94	2.84	3.03	2.95	1.47	130	0.23	0.19
3	0.02	1000	7.9	2.63	2.71	2.62	2.89	2.71	1.53	147	0.13	0.10
4	0.02	1200	8.4	2.22	2.38	2.40	2.71	2.43	1.72	140	0.03	0.04
5	0.04	1500	7.9	2.94	2.86	2.65	2.86	2.83	1.50	128	0.18	0.14
6	0.04	2000	8.4	2.60	2.64	2.57	2.69	2.63	1.66	140	0.10	0.06
7	0.04	2500	8.4	2.45	2.55	2.54	2.78	2.58	1.67	137	0.08	0.05
8	0.04	3000	8.4	2.04	2.55	2.69	2.97	2.56	1.68	142	0.07	0.04
9	0.06	12000	7.9	3.21	3.12	3.00	3.12	3.11	1.43	138	0.30	0.25
10	0.06	8000	7.9	3.31	3.22	3.20	3.50	3.31	1.39	124	0.38	0.33
11	0.06	9000	8.4	3.38	3.26	3.16	3.39	3.30	1.48	128	0.37	0.33
12	0.06	10000	7.9	3.19	3.09	2.97	3.22	3.12	1.43	135	0.30	0.25
13	0.06	14000	8.4	2.62	2.59	2.67	2.95	2.71	1.63	135	0.13	0.09
14	0.01	800	8.4	2.62	2.69	2.56	2.87	2.69	1.64	138	0.12	0.08
15	0.01	1000	8.4	2.18	2.33	2.49	2.84	2.46	1.71	138	0.04	0.03
16	0.01	1200	8.9	1.90	2.35	2.68	3.26	2.55	1.78	142	0.11	0.09
17	0.03	1000	7.9	2.94	2.87	2.70	3.04	2.89	1.48	139	0.21	0.16
18	0.03	1500	8.4	2.46	2.59	2.49	2.78	2.58	1.67	144	0.08	0.05
19	0.03	2000	8.9	2.07	2.53	2.71	2.97	2.57	1.77	145	0.11	0.09
20	0.03	2500	9.6	1.95	2.31	2.65	3.05	2.49	1.94	136	0.18	0.17
21	0.04	3500	8.9	1.71	2.12	2.66	3.04	2.38	1.84	136	0.09	0.10
22	0.05	8000	8.9	1.70	2.13	2.51	2.91	2.31	1.87	137	0.10	0.11
23	0.05	10000	8.9	2.04	2.48	2.77	3.10	2.60	1.76	137	0.12	0.10
24	0.05	12000	8.9	1.77	2.45	2.94	3.35	2.63	1.75	136	0.13	0.10
25	0.05	14000	8.9	1.82	2.06	2.55	3.27	2.43	1.82	136	0.09	0.09
26	0.05	6000	8.4	2.16	2.54	2.59	2.80	2.52	1.69	146	0.06	0.03
27	0.06	16000	8.4	2.87	2.73	2.70	2.94	2.81	1.60	133	0.17	0.13
28	0.04	4000	8.9	1.99	2.48	2.70	3.12	2.57	1.77	139	0.11	0.09
29	0.02	1600	7.6	2.09	2.47	2.65	3.13	2.59	1.51	139	0.10	0.08
30	0.02	4000	11.2	1.99	1.93	2.19	2.42	2.13	2.45	152	0.39	0.40
31	0.04	3200	8.9	1.80	2.29	2.65	3.00	2.44	1.82	135	0.09	0.09
32	0.05	7000	8.4	1.77	2.42	2.67	2.93	2.45	1.71	139	0.03	0.03
33	0.06	15000	7.9	2.62	2.58	2.71	3.05	2.74	1.52	137	0.15	0.11

Appendix D: Details on the modelling approach

Information on the number of model runs, the intervals between the μ - and ξ -values upon modelling, and event-specific and general input values that were used upon modelling. Appendix B also lists the results of the model runs per event where the model results and observations had a best fit.

Number of model runs

Event	# of simulations	best z-value
21.06.19	43	0.06
02.07.19	34	0.32
11.08.19	41	0.13
20.08.19	36	0.02
24.06.21	37	0.03
06.07.21	38	0.03
16.07.21	30	0.03
07.08.21	23	0.23
19.09.21	33	0.11
05.06.22	12	0.01
04.07.22	13	0.02
08.09.22	20	0.34
Total	360	

Variations of μ and ξ values

μ	0.01
ξ	1 to > 1000

For μ we only used the values 0.01, 0.02, 0.03, 0.04, 0.05 and 0.06 upon modelling.

Also upon modeling, the intervals between the ξ -values were 1 for those models where we set $\mu=1$. For larger μ -values, we increased the intervals between the subsequent ξ -values to $\gg 1000$. We iteratively changed the values until we found a best-fit between model results and observations.

Input for RAMMS, which were not event-specific

DTM	DTM_0.5.tif
DTM resolution [m]	0.5
calculation domain	calcdom.shp
release area	hydrograph.shp
stop parameter [%]	5
sim resolution [m]	0.5
end time [s]	1000
dump step [s]	2
erosion layer	erosion.shp
erosion density [kg/m ³]	2000
erosion rate [m/s]	0.025
pot. Erosion depth [per kPa]	0.1
critical shear stress [kPa]	1
max erosion depth [m]	1
inflow direction [°]	60
t1 Hydrograph [s]	10

Input for RAMMS, which were event-specific

Event	21.06.19	02.07.19	11.08.19	20.08.19	24.06.21	06.07.21	16.07.21	07.08.21	19.09.21	05.06.22	04.07.22	08.09.22
density [kg/m ³]	1870	1971	2323	2031	1750	1605	1916	1884	1697	1690	1189	1592
vol [m ³]	97394	73188	88064	6137	105032	76906	80879	38737	8538	39498	175929	9283
Qmax [m ³ /s]	147.61	65.58	95.63	8.06	162.2	186.61	60.7	41.19	10.67	55.42	169.14	20.94
Front velocity CD 28-29 [m/s]	6.62	3.86	6.95	0.89	8.18	8.69	2.78	2.32	1.25	3.39	8.18	1.91
Max flow depth laser [m]	3.13	1.75	1.81	1.13	2.4	2.5	2.38	2.49	1.13	2.08	2.49	1.93
Max flow depth radar [m]	2.69	1.73	1.89	1.1	2.49	2.58	2.44	2.17	1.22	2.15	2.6	1.77
Froude Number	1.19	0.93	1.65	0.27	1.69	1.75	0.58	0.47	0.38	0.75	1.66	0.44

Best-fit outputs of RAMMs models

Event	21.06.19	02.07.19	11.08.19	20.08.19	24.06.21	06.07.21	16.07.21	07.08.21	19.09.21	05.06.22	04.07.22	08.09.22
Front velocity CD 28-29 [m/s]	6.7	3.9	7.4	0.9	8.4	8.9	2.8	2.31	1.24	3.35	8.38	1.76
Max flow depth [m]	2.96	2.32	2.02	1.15	2.43	2.47	2.32	1.91	1.01	2.09	2.5	1.29
Froude number	1.24	0.83	1.66	0.27	1.72	1.81	0.59	0.53	0.39	0.74	1.69	0.49
Qmax [m ³ /s]	122	54	78	7	140	158	48	35	9	40	143	17
μ	0.06	0.06	0.06	0.01	0.02	0.05	0.05	0.04	0.01	0.06	0.01	0.01
ξ	4500	1000	8500	12	1200	10000	170	105	25	700	1000	50
z-value	0.06	0.32	0.13	0.02	0.03	0.03	0.03	0.23	0.11	0.01	0.02	0.34

Appendix E: Measured and calculated properties for each flow (v, flow depth, Froude number, volume, density), best-fit model results (μ , ξ , z) and related total (S) and Coulomb and turbulent frictions

For each debris flow event, distinct μ - ξ pairs can be used to successfully model the flow properties such as flow velocity and flow depth. The best-fit solutions between model results and observations, characterized by the lowest z-values, are highlighted by the yellow bar. The values of these best-fit results are displayed in Table E.

Event	v [m/s]	Flow Depth [m]	Froude Number	Volume (m ³)	Density (kg/m ³)	μ	ξ	z	Total Friction S [Pa]	Coulomb Friction [Pa]	Turbulent Friction [Pa]	Coulomb Friction [%]	Turbulent Friction [%]
21.06.19	6.6	3.1	1.19	97394	1870	0.01	500	0.07	2166	568	1598	26	74
21.06.19	6.6	3.1	1.19	97394	1870	0.02	550	0.10	2588	1135	1453	44	56
21.06.19	6.6	3.1	1.19	97394	1870	0.03	800	0.10	2702	1703	999	63	37
21.06.19	6.6	3.1	1.19	97394	1870	0.04	1000	0.11	3069	2270	799	74	26
21.06.19	6.6	3.1	1.19	97394	1870	0.05	1300	0.11	3452	2838	615	82	18
21.06.19	6.6	3.1	1.19	97394	1870	0.06	4500	0.06	3583	3405	178	95	5
02.07.19	3.9	1.8	0.93	73188	1971	0.01	200	0.37	1818	347	1470	19	81
02.07.19	3.9	1.8	0.93	73188	1971	0.02	250	0.37	1871	695	1176	37	63
02.07.19	3.9	1.8	0.93	73188	1971	0.03	300	0.37	2022	1042	980	52	48
02.07.19	3.9	1.8	0.93	73188	1971	0.04	350	0.36	2230	1389	840	62	38
02.07.19	3.9	1.8	0.93	73188	1971	0.05	600	0.35	2227	1737	490	78	22
02.07.19	3.9	1.8	0.93	73188	1971	0.06	1000	0.32	2378	2084	294	88	12
11.08.19	7	1.8	1.65	88064	2323	0.01	1000	0.16	1526	409	1117	27	73
11.08.19	7	1.8	1.65	88064	2323	0.02	1000	0.18	1935	819	1117	42	58
11.08.19	7	1.8	1.65	88064	2323	0.03	2500	0.21	1675	1228	447	73	27
11.08.19	7	1.8	1.65	88064	2323	0.04	2000	0.18	2196	1637	558	75	25
11.08.19	7	1.8	1.65	88064	2323	0.05	8000	0.14	2186	2047	140	94	6
11.08.19	7	1.8	1.65	88064	2323	0.06	8500	0.13	2588	2456	131	95	5
20.08.19	0.9	1.1	0.27	6137	2031	0.01	12	0.02	1564	219	1345	14	86
20.08.19	0.9	1.1	0.27	6137	2031	0.02	13	0.03	1679	437	1241	26	74
20.08.19	0.9	1.1	0.27	6137	2031	0.03	12	0.10	2001	656	1345	33	67
20.08.19	0.9	1.1	0.27	6137	2031	0.04	21	0.12	1643	875	769	53	47
20.08.19	0.9	1.1	0.27	6137	2031	0.05	20	0.17	1901	1094	807	58	42
20.08.19	0.9	1.1	0.27	6137	2031	0.06	30	0.25	1850	1312	538	71	29
24.06.21	8.2	2.4	1.69	105032	1750	0.01	1000	0.04	1566	411	1154	26	74
24.06.21	8.2	2.4	1.69	105032	1750	0.02	1200	0.03	1784	822	962	46	54
24.06.21	8.2	2.4	1.69	105032	1750	0.03	1500	0.08	2003	1234	770	62	38
24.06.21	8.2	2.4	1.69	105032	1750	0.04	3000	0.07	2030	1645	385	81	19
24.06.21	8.2	2.4	1.69	105032	1750	0.05	7000	0.03	2221	2056	165	93	7
24.06.21	8.2	2.4	1.69	105032	1750	0.06	14000	0.13	2550	2467	82	97	3
06.07.21	8.7	2.5	1.75	76906	1605	0.01	800	0.06	1883	393	1490	21	79
06.07.21	8.7	2.5	1.75	76906	1605	0.02	1500	0.06	1580	786	794	50	50
06.07.21	8.7	2.5	1.75	76906	1605	0.03	1750	0.08	1860	1179	681	63	37
06.07.21	8.7	2.5	1.75	76906	1605	0.04	3000	0.09	1969	1571	397	80	20
06.07.21	8.7	2.5	1.75	76906	1605	0.05	10000	0.03	2083	1964	119	94	6
06.07.21	8.7	2.5	1.75	76906	1605	0.06	25000	0.12	2405	2357	48	98	2
16.07.21	2.8	2.4	0.58	80879	1916	0.01	65	0.04	2717	450	2267	17	83
16.07.21	2.8	2.4	0.58	80879	1916	0.02	75	0.04	2865	900	1965	31	69
16.07.21	2.8	2.4	0.58	80879	1916	0.03	95	0.05	2902	1351	1551	47	53
16.07.21	2.8	2.4	0.58	80879	1916	0.04	125	0.07	2980	1801	1179	60	40
16.07.21	2.8	2.4	0.58	80879	1916	0.05	170	0.03	3118	2251	867	72	28
16.07.21	2.8	2.4	0.58	80879	1916	0.06	280	0.04	3227	2701	526	84	16

07.08.21	2.3	2.5	0.47	38737	1884	0.01	50	0.25	2417	461	1955	19	81
07.08.21	2.3	2.5	0.47	38737	1884	0.02	65	0.26	2426	922	1504	38	62
07.08.21	2.3	2.5	0.47	38737	1884	0.03	65	0.25	2888	1383	1504	48	52
07.08.21	2.3	2.5	0.47	38737	1884	0.04	105	0.23	2776	1845	931	66	34
07.08.21	2.3	2.5	0.47	38737	1884	0.05	150	0.25	2957	2306	652	78	22
07.08.21	2.3	2.5	0.47	38737	1884	0.06	230	0.27	3192	2767	425	87	13
19.09.21	1.3	1.1	0.38	8538	1697	0.01	25	0.11	1308	183	1125	14	86
19.09.21	1.3	1.1	0.38	8538	1697	0.02	30	0.12	1303	366	938	28	72
19.09.21	1.3	1.1	0.38	8538	1697	0.03	43	0.17	1203	548	654	46	54
19.09.21	1.3	1.1	0.38	8538	1697	0.04	50	0.18	1294	731	563	57	43
19.09.21	1.3	1.1	0.38	8538	1697	0.05	80	0.23	1265	914	352	72	28
19.09.21	1.3	1.1	0.38	8538	1697	0.06	160	0.20	1272	1097	176	86	14
05.06.22	3.4	2.1	0.75	39498	1690	0.01	130	0.06	1822	347	1474	19	81
05.06.22	3.4	2.1	0.75	39498	1690	0.02	160	0.05	1893	695	1198	37	63
05.06.22	3.4	2.1	0.75	39498	1690	0.03	210	0.05	1955	1042	913	53	47
05.06.22	3.4	2.1	0.75	39498	1690	0.04	260	0.04	2127	1390	737	65	35
05.06.22	3.4	2.1	0.75	39498	1690	0.05	400	0.03	2216	1737	479	78	22
05.06.22	3.4	2.1	0.75	39498	1690	0.06	700	0.01	2359	2085	274	88	12
04.07.22	8.2	2.5	1.66	175929	1189	0.01	1000	0.02	1075	291	784	27	73
04.07.22	8.2	2.5	1.66	175929	1189	0.02	1200	0.04	1236	582	654	47	53
04.07.22	8.2	2.5	1.66	175929	1189	0.03	1500	0.07	1396	873	523	63	37
04.07.22	8.2	2.5	1.66	175929	1189	0.04	2000	0.09	1556	1164	392	75	25
04.07.22	8.2	2.5	1.66	175929	1189	0.05	6000	0.04	1586	1455	131	92	8
04.07.22	8.2	2.5	1.66	175929	1189	0.06	20000	0.08	1785	1746	39	98	2
08.09.22	1.9	1.9	0.44	9283	1592	0.01	50	0.34	1424	296	1128	21	79
08.09.22	1.9	1.9	0.44	9283	1592	0.02	60	0.36	1532	592	940	39	61
08.09.22	1.9	1.9	0.44	9283	1592	0.03	80	0.37	1593	888	705	56	44
08.09.22	1.9	1.9	0.44	9283	1592	0.04	125	0.39	1636	1185	451	72	28
08.09.22	1.9	1.9	0.44	9283	1592	0.05	150	0.35	1857	1481	376	80	20
08.09.22	1.9	1.9	0.44	9283	1592	0.06	350	0.41	1938	1777	161	92	8

Appendix F: Best-fit model results per event

Each debris flow event can be characterized by a distinct μ - ξ pair with a lowest z-value. See Table in Appendix B for best-fit μ - ξ pairs per event.

Event	v [m/s]	Flow Depth [m]	Froude Number	Volume (m ³)	Density (kg/m ³)	μ	ξ	z	Total Friction [Pa]	Coulomb Friction [Pa]	Turbulent Friction [Pa]	Coulomb Friction [%]	Turbulent Friction [%]
21.06.19	6.6	3.1	1.19	97394	1870	0.06	4500	0.06	3583	3405	178	95	5
02.07.19	3.9	1.8	0.93	73188	1971	0.06	1000	0.32	2378	2084	294	88	12
11.08.19	7	1.8	1.65	88064	2323	0.06	8500	0.13	2588	2456	131	95	5
20.08.19	0.9	1.1	0.27	6137	2031	0.01	12	0.02	1564	219	1345	14	86
24.06.21	8.2	2.4	1.69	105032	1750	0.02	1200	0.03	1784	822	962	46	54
06.07.21	8.7	2.5	1.75	76906	1605	0.05	10000	0.03	2083	1964	119	94	6
16.07.21	2.8	2.4	0.58	80879	1916	0.05	170	0.03	3118	2251	867	72	28
07.08.21	2.3	2.5	0.47	38737	1884	0.04	105	0.23	2776	1845	931	66	34
19.09.21	1.3	1.1	0.38	8538	1697	0.01	25	0.11	1308	183	1125	14	86
05.06.22	3.4	2.1	0.75	39498	1690	0.06	700	0.01	2359	2085	274	88	12
04.07.22	8.2	2.5	1.66	175929	1189	0.01	1000	0.02	1075	291	784	27	73
08.09.22	1.9	1.9	0.44	9283	1592	0.01	50	0.34	1424	296	1128	21	79

Event		21.06.19			02.07.19			26.07.19			11.08.19			20.08.19		
Sample mass [g]		1958.7			1772.4			2856.1			3299.7			3001.5		
Method	Mesh size [mm]	Weight [g]	Weight % passing	Weight % passing max. 16 mm	Weight [g]	Weight % passing	Weight % passing max. 16 mm	Weight [g]	Weight % passing	Weight % passing max. 16 mm	Weight [g]	Weight % passing	Weight % passing max. 16 mm	Weight [g]	Weight % passing	Weight % passing max. 16 mm
dry sieving	125.0000	0.0	100.0	100.0	0.0	100.0	100.0	0.0	100.0	100.0	0.0	100.0	100.0	0.0	100.0	100.0
	63.0000	0.0	100.0	100.0	0.0	100.0	100.0	0.0	100.0	100.0	0.0	100.0	100.0	0.0	100.0	100.0
	31.5000	0.0	100.0	100.0	0.0	100.0	100.0	55.7	98.1	100.0	0.0	100.0	100.0	0.0	100.0	100.0
	16.0000	365.0	81.4	100.0	0.0	100.0	100.0	158.9	92.5	100.0	472.6	85.7	100.0	327.9	89.1	100.0
	8.0000	239.7	69.1	85.0	3.4	99.8	99.8	308.3	81.7	88.3	380.6	74.1	86.5	341.7	77.7	87.2
	4.0000	180.2	59.9	73.7	40.5	97.5	97.5	258.1	72.7	78.6	288.3	65.4	76.3	287.4	68.1	76.5
	2.0000	122.5	53.7	66.0	88.3	92.5	92.5	199.3	65.7	71.0	220.4	58.7	68.5	198.8	61.5	69.0
	1.0000	110.5	48.0	59.0	123.6	85.6	85.6	189.9	59.0	63.8	211.7	52.3	61.1	184.7	55.3	62.1
wet sieving	0.5000	111.4	42.3	52.0	142.0	77.6	77.6	187.3	52.5	56.7	206.6	46.1	53.8	182.5	49.3	55.3
	0.2500		36.4	44.8		68.6	68.6		45.0	48.6		42.9	50.1		42.6	47.8
	0.1250		30.6	37.6		59.0	59.0		38.2	41.3		37.7	44.0		36.2	40.6
slurry test	0.0630		25.8	31.7		49.1	49.1		31.8	34.4		31.1	36.3		30.4	34.1
	0.0462		23.0	28.3		44.4	44.4		28.2	30.5		27.9	32.6		27.4	30.7
	0.0339		20.2	24.8		39.6	39.6		24.2	26.1		24.2	28.3		24.0	27.0
	0.0224		15.8	19.4		30.8	30.8		18.6	20.1		18.4	21.5		18.3	20.6
	0.0135		10.6	13.0		21.3	21.3		12.3	13.3		12.0	14.0		12.8	14.4
	0.0081		6.4	7.9		12.5	12.5		7.4	8.0		7.2	8.4		7.9	8.9
	0.0050		4.1	5.1		7.8	7.8		4.9	5.3		4.6	5.4		5.1	5.7
	0.0032		2.6	3.2		4.8	4.8		3.2	3.5		3.1	3.6		3.3	3.7
0.0015		1.1	1.3		2.5	2.5		1.7	1.8		1.4	1.6		1.9	2.1	
0.0000		0.0	0.0		0.0	0.0		0.0	0.0		0.0	0.0		0.0	0.0	

Event		24.06.21			06.07.21			16.07.21			07.08.21			19.09.21		
Sample mass [g]		2652.5			3341.9			2511.2			2965.8			2553.6		
Method	Mesh size [mm]	Weight [g]	Weight % passing	Weight % passing max. 16 mm	Weight [g]	Weight % passing	Weight % passing max. 16 mm	Weight [g]	Weight % passing	Weight % passing max. 16 mm	Weight [g]	Weight % passing	Weight % passing max. 16 mm	Weight [g]	Weight % passing	Weight % passing max. 16 mm
dry sieving	125.0000	0.0	100.0	100.0	0.0	100.0	100.0	0.0	100.0	100.0	0.0	100.0	100.0	0.0	100.0	100.0
	63.0000	0.0	100.0	100.0	0.0	100.0	100.0	0.0	100.0	100.0	0.0	100.0	100.0	0.0	100.0	100.0
	31.5000	0.0	100.0	100.0	296.0	83.3	100.0	434.0	84.8	100.0	602.3	81.7	100.0	212.2	92.9	100.0
	16.0000	102.7	94.8	100.0	290.2	66.9	100.0	615.7	63.2	100.0	795.1	57.7	100.0	405.6	79.4	100.0
	8.0000	152.8	87.0	91.8	163.4	57.7	86.2	349.9	51.0	80.6	279.6	49.2	85.3	261.1	70.7	89.0
	4.0000	151.6	79.2	83.6	131.8	50.3	75.1	200.7	44.0	69.5	199.4	43.1	74.8	217.9	63.5	79.9
	2.0000	127.9	72.7	76.7	84.7	45.5	68.0	116.3	39.9	63.1	119.0	39.5	68.6	151.8	58.4	73.5
	1.0000	125.9	66.3	69.9	81.8	40.9	61.1	80.2	37.1	58.6	102.7	36.4	63.2	139.3	53.8	67.7
wet sieving	0.5000	138.8	59.2	62.5	87.4	35.9	53.7	76.7	34.4	54.4	106.6	33.2	57.6	162.5	48.3	60.9
	0.2500		50.9	53.7		31.2	46.7		31.0	49.0		29.3	50.7		41.6	52.4
	0.1250		42.5	44.9		26.2	39.1		26.6	42.1		25.0	43.4		34.6	43.6
slurry test	0.0630		35.1	37.0		21.4	32.0		22.4	35.4		20.7	35.9		28.3	35.7
	0.0462		31.5	33.2		19.2	28.7		20.3	32.2		18.6	32.3		25.5	32.1
	0.0339		27.4	28.9		16.4	24.5		17.7	28.0		15.9	27.7		21.5	27.0
	0.0224		21.7	22.9		12.7	18.9		14.0	22.1		12.5	21.7		16.2	20.4
	0.0135		14.4	15.2		8.7	13.0		9.5	15.1		8.3	14.4		10.7	13.4
	0.0081		8.4	8.9		4.8	7.1		6.0	9.5		5.0	8.6		6.4	8.0
	0.0050		5.4	5.7		3.0	4.5		3.6	5.8		2.9	5.0		4.0	5.0
	0.0032		3.6	3.8		2.1	3.1		2.6	4.1		1.9	3.4		2.5	3.2
0.0015		2.3	2.4		1.3	1.9		1.4	2.2		0.9	1.5		1.4	1.8	
0.0000		0.0	0.0		0.0	0.0		0.0	0.0		0.0	0.0		0.0	0.0	

Event		04.10.21			05.06.22			04.07.22			08.09.22		
Sample mass [g]		2788.3			2866.9			2677.2			3400.6		
Method	Mesh size [mm]	Weight [g]	Weight % passing	Weight % passing max. 16 mm	Weight [g]	Weight % passing	Weight % passing max. 16 mm	Weight [g]	Weight % passing	Weight % passing max. 16 mm	Weight [g]	Weight % passing	Weight % passing max. 16 mm
dry sieving	125.0000	0.0	100.0	100.0	0.0	100.0	100.0	0.0	100.0	100.0	0.0	100.0	100.0
	63.0000	0.0	100.0	100.0	0.0	100.0	100.0	0.0	100.0	100.0	0.0	100.0	100.0
	31.5000	147.8	92.5	100.0	116.2	93.4	100.0	315.5	89.0	100.0	167.8	94.9	100.0
	16.0000	284.9	77.9	100.0	312.6	75.8	100.0	553.6	69.6	100.0	527.1	78.9	100.0
	8.0000	180.9	68.7	88.1	182.8	65.5	86.4	364.6	56.8	81.7	406.8	66.6	84.4
	4.0000	128.7	62.1	79.7	109.5	59.3	78.2	221.3	49.1	70.5	256.4	58.8	74.5
	2.0000	92.4	57.4	73.7	90.7	54.2	71.5	145.4	44.0	63.2	168.7	53.7	68.1
	1.0000	78.2	53.4	68.5	93.5	48.9	64.5	126.4	39.5	56.8	162.7	48.8	61.8
wet sieving	0.5000	89.8	48.8	62.6	106.9	42.9	56.6	132.2	34.9	50.2	181.1	43.3	54.9
	0.2500		43.7	56.1		37.0	48.8		30.1	43.2		37.5	47.5
	0.1250		37.2	47.8		31.5	41.5		24.9	35.8		31.9	40.4
slurry test	0.0630		31.0	39.8		25.8	34.0		20.4	29.4		26.1	33.0
	0.0462		28.0	36.0		22.6	29.8		18.3	26.3		23.1	29.3
	0.0339		23.8	30.5		19.5	25.7		15.9	22.8		20.4	25.8
	0.0224		18.4	23.6		15.1	19.9		12.1	17.3		16.1	20.4
	0.0135		12.3	15.8		10.0	13.2		8.4	12.0		10.3	13.0
	0.0081		7.4	9.5		6.3	8.3		4.9	7.1		6.2	7.9
	0.0050		4.6	5.9		4.1	5.4		3.4	4.8		4.2	5.3
	0.0032		3.1	4.0		2.9	3.8		2.5	3.5		3.0	3.9
0.0015		2.2	2.8		1.8	2.3		1.3	1.9		1.8	2.3	
0.0000		0.0	0.0		0.0	0.0		0.0	0.0		0.0	0.0	

Appendix H: Results of powder x-ray diffraction analysis

Measured weight percent per mineral for all four analyzed samples.

	02.07.2019	26.07.2019	20.08.2019	16.07.2021
Albite	2.0	2.0	1.8	2.0
Calcite	10.6	7.4	10.2	17.9
Dolomite	24.4	16.7	23.7	19.4
Muscovite	17.7	22.2	19.6	18.2
Orthoclase	3.4	2.9	2.8	3.0
Quartz	29.9	36.0	29.2	30.9
Chlorite	0.3	0.1	0.2	0.0
Illite	11.3	12.1	11.7	8.4
Kaolinite	0.0	0.1	0.1	0.0
Smektite	0.2	0.6	0.7	0.3